AGU PUBLICATIONS

JGR

Journal of Geophysical Research: Atmospheres

RESEARCH ARTICLE

10.1002/2015JD024142

Key Points:

- Future wildfire activity increases in the extratropics and decreases in the tropics
- Changes in wildfire activity compensate decreasing anthropogenic emissions
- Future changes in emissions heights are negligible for the climate impact

Correspondence to:
A. Veira,
andreas.veira@mpimet.mpg.de

Citation:
Veira, A., G. Lasslop, and S. Kloster (2016), Wildfires in a warmer climate: Emission fluxes, emission heights, and black carbon concentrations in 2090–2099, *J. Geophys. Res. Atmos.*, *121*, 3195–3223, doi:10.1002/2015JD024142.

Received 27 AUG 2015
Accepted 7 MAR 2016
Accepted article online 11 MAR 2016
Published online 8 APR 2016

Wildfires in a warmer climate: Emission fluxes, emission heights, and black carbon concentrations in 2090–2099

A. Veira[1,2], G. Lasslop[1], and S. Kloster[1]

[1] Max Planck Institute for Meteorology, Hamburg, Germany, [2] International Max Planck Research School on Earth System Modelling, Hamburg, Germany

Abstract Global warming is expected to considerably impact wildfire activity and aerosol emission release in the future. Due to their complexity, the future interactions between climate change, wildfire activity, emission release, and atmospheric aerosol processes are still uncertain. Here we use the process-based fire model SPITFIRE within the global vegetation model JSBACH to simulate wildfire activity for present-day climate conditions and future Representative Concentration Pathways (RCPs). The modeled fire emission fluxes and fire radiative power serve as input for the aerosol-climate model ECHAM6-HAM2, which has been extended by a semiempirical plume height parametrization. Our results indicate a general increase in extratropical and a decrease in tropical wildfire activity at the end of the 21st century. Changes in emission fluxes are most pronounced for the strongest warming scenario RCP8.5 (+49% in the extratropics, −37% in the tropics). Tropospheric black carbon (BC) concentrations are similarly affected by changes in emission fluxes and changes in climate conditions with regional variations of up to −50% to +100%. In the Northern Hemispheric extratropics, we attribute a mean increase in aerosol optical thickness of $+0.031\pm0.002$ to changes in wildfire emissions. Due to the compensating effects of fire intensification and more stable atmospheric conditions, global mean emission heights change by at most 0.3 km with only minor influence on BC long-range transport. The changes in wildfire emission fluxes for the RCP8.5 scenario, however, may largely compensate the projected reduction in anthropogenic BC emissions by the end of the 21st century.

1. Introduction

Although wildfires are known to be a major vegetation disturbance and aerosol emission source, our scientific understanding of wildfires as an integrated part of the Earth system is rather low [*Bowman et al.*, 2009; *Langmann et al.*, 2009; *Keywood et al.*, 2013]. While there is agreement about an expected future decrease in carbonaceous aerosol emissions from anthropogenic sources [*Lamarque et al.*, 2011; *Bond et al.*, 2013; *Shindell et al.*, 2013], the future trend in aerosol emissions from wildfires is much more uncertain. This is due to the fact that the interactions between fire, land, and atmosphere are very complex. First integrated approaches to assess post-fire changes in albedo, radiative forcing of emitted aerosols and subsequent feedbacks on climate have shown that the processes relevant for wildfire-climate interactions cover several magnitudes of temporal and spatial scales [*Stavros et al.*, 2014, and references therein]. However, the ability of state-of-the-art Earth system models to appropriately simulate vegetation fire-climate interactions is very limited [*Carslaw et al.*, 2010; *Ciais et al.*, 2013; *Reichstein et al.*, 2013]. To investigate the future climate impact of wildfires, we are in need of an improved coupling between vegetation dynamics, wildfire activity, emissions, and atmospheric aerosol transport. At the interface of terrestrial and atmospheric processes, emission heights are of particular importance, because they determine the impact of fire emissions on climate due to their influence on aerosol long-range transport, aerosol-cloud interaction, and radiation [*Luderer et al.*, 2006; *Samset et al.*, 2013; *Veira et al.*, 2015a]. On the other hand, emission heights themselves are strongly impacted by atmospheric stability and fire intensity, which are both expected to change in the future [e.g., *Joshi et al.*, 2007; *Luo et al.*, 2013].

While a general increase in burned area and fire occurrence in the extratropics during the 21st century was indicated by most previous studies [e.g., *Flannigan et al.*, 2009, and references therein], the magnitude of the changes remains uncertain. In the tropics, changes in wildfire activity have been projected to be less pronounced, but regionally strong enhancements as well as reductions in fire activity have been simulated [e.g., *Liu et al.*, 2010; *Flannigan et al.*, 2013].

As most of the future fire probability projections are based on atmospheric parameters only, no wildfire emission estimates are provided, because these require vegetation-specific information on the biomass available for burning. Therefore, recent efforts aim to implement process-based fire models into dynamic global vegetation models (DGVMs) allowing for interactive trace gas and aerosol emission estimates. The fire model SPITFIRE, for example, has been implemented into LPJ [*Pfeiffer et al.*, 2013], JSBACH [*Lasslop et al.*, 2014], and Organizing Carbon and Hydrology in Dynamic Ecosystems (ORCHIDEE) [*Yue et al.*, 2014].

However, up to now, the radiative forcing of aerosol emissions from wildfires has primarily been investigated for present-day (PD) climate conditions based on prescribed, satellite-based wildfire emission inventories [e.g., *Myhre et al.*, 2009; *Unger et al.*, 2010; *Veira et al.*, 2015a]. The total wildfire top of atmosphere radiative forcing in current state-of-the-art climate-aerosol models ranges between $+0.18 \pm 0.10$ W m^{-2} [*Tosca et al.*, 2013] and -0.29 ± 0.07 W m^{-2} [*Jones et al.*, 2007].

In contrast to the prescribed wildfire emission inventories used in the studies mentioned above, *Ward et al.* [2012] applied interactively simulated wildfire emission estimates based on a fire model by *Kloster et al.* [2012] and provided a first assessment of simulated wildfire activity, emission release, and radiative forcing for the years 1850, 2000, and 2100. The authors found that fire emissions produce an overall negative radiative forcing for all time periods, but the contribution of trace gases and aerosols varies.

To our knowledge, up to now the impact of climate-induced changes in emission heights and their influence on atmospheric black carbon (BC) has not yet been investigated. *Veira et al.* [2015b] and *Veira et al.* [2015a] implemented a semiempirical plume height parametrization in a global aerosol-climate model and, for the first time, quantified the global emission height impact on atmospheric aerosol long-range transport and top of atmosphere as well as surface net radiation for PD climate conditions.

In the present study, we integrate fire emission estimates and interactively calculate fire emission heights for future climate conditions and quantify the impact of changes in emission fluxes and emission heights on atmospheric aerosol concentrations. Our study aims to investigate the question, how wildfire emission fluxes might change in the future and to what extent the changes in atmospheric conditions and changes in fire intensity might impact fire emission heights. Furthermore, we disentangle how atmospheric BC concentrations respond to changes in wildfire emission fluxes, changes in emission heights, and changes in atmospheric conditions. In addition, we try to estimate the magnitude of changes in aerosol optical thickness (AOT) which is induced by changes in climate conditions and changes in emission fluxes.

To answer these questions, we use the process-based fire model SPITFIRE within the global vegetation model JSBACH and simulate global wildfire activity, fire intensity, and emission fluxes for different Representative Concentration Pathway (RCP) scenarios in the 21st century. In a second step, we apply the global aerosol-climate model ECHAM6-HAM2 extended by a semiempirical plume height parametrization with JSBACH-SPITFIRE emissions as boundary conditions to simulate aerosol transport, deposition rates, and AOT for different RCP scenarios between 2090 and 2099. A range of sensitivity experiments allows us to disentangle the impacts of future changes in climate conditions, emission heights, and emission fluxes on the atmospheric aerosol concentrations and AOT.

The next chapter introduces the specific model components and describes the simulation setup. In the results section, we analyze the contributions of changes in emission fluxes and emission heights on changes in simulated atmospheric BC concentrations and AOT at the end of the 21st century. In the conclusions section we summarize our findings and provide suggestions for future improvements in the representation of vegetation fire-aerosol climate interactions in Earth system models.

2. Methodology

In the following we introduce the DGVM and the atmospheric aerosol model, which are used to investigate wildfire emission fluxes and related atmospheric aerosol concentrations in a warmer future climate. Moreover, we describe the implementation of wildfire emission heights and the anthropogenic emission inventories applied in this study.

2.1. JSBACH-SPITFIRE Model Description

All fire-related processes and fire emission fluxes in this study are simulated by JSBACH-SPITFIRE [*Lasslop et al.*, 2014] which is an implementation of SPITFIRE [*Thonicke et al.*, 2010] in JSBACH [*Brovkin et al.*, 2013;

Reick et al., 2013; *Schneck et al.*, 2013]. JSBACH is the land component of the Max Planck Institute Earth System Model (MPI-ESM) [*Giorgetta et al.*, 2013]. SPITFIRE is a process-based fire model which simulates fires based on guiding physical principles. The number of natural and human ignitions is combined with the rate of fire spread and the fire duration to estimate the burned area. Based on the biomass burned, SPITFIRE calculates daily total carbon emissions which are transformed into aerosol emissions following vegetation-specific emission factors [*Akagi et al.*, 2011].

JSBACH-SPITFIRE is run on a T63 grid (approximately 1.9° × 1.9°) as described in *Lasslop et al.* [2014], but for our simulations the dependency of fire size on population density is based on a linear decreasing relationship between population density and observed mean fire size in Moderate Resolution Imaging Spectroradiometer (MODIS) data [*Hantson et al.*, 2015]. The decrease in mean fire size with increasing population density is explained by the landscape fragmentation which inhibits fire spread in more densely populated areas, for details of the parametrization see *Hantson et al.* [2015]. Moreover, the diagnostic parameter total fire radiative power (FRP) of all fires in a particular grid cell was implemented. The variable FRP is globally available from satellite-based measurements which have been used for the calculation of wildfire emission heights by *Sofiev et al.* [2012]. We consider that only the fuel classes 1 h to 100 h (representing leaves, small branches, and large branches) contribute to the flaming process, but not the 1000 h fuel class (representing trunks). The fuel classes describe the time which is required to reduce the moisture of a fuel particle by 67% for specific ambient conditions (80°F and 20% relative humidity) [*Keane*, 2015]. In SPITFIRE, the consumed fuel $f_{1-100\mathrm{h}}$ of the fuel classes 1 h to 100 h is a function of the biomass available for burning, the fuel moisture, and the wind speed. For a more detailed description see Appendix A of *Thonicke et al.* [2010] and *Lasslop et al.* [2014]. Following the average consumed fuel per unit area (g biomass m^{-2}) simulated by JSBACH-SPITFIRE and assuming a constant heat capacity h, we derive the diagnostic variable mean daily FRP:

$$\mathrm{FRP} = \alpha \cdot \frac{f_{1-100\mathrm{h}}}{86400\,s} \cdot A \cdot h, \tag{1}$$

where α describes the fraction of energy which is released as radiation. Here we choose a globally constant value of $\alpha = 0.15$ based on the references by *Wooster et al.* [2005], *Freeborn et al.* [2008], *Kremens et al.* [2012], *Morandini et al.* [2013], and *Smith et al.* [2013], which provide values for α that range between 0.12 and 0.17 for different vegetation types. The uncertainty of the globally constant α value can be assumed to be as large as the measurement range, but due to the plant functional type (PFT) concept applied in the JSBACH model, a more accurate application of the measured species-specific α values is not applicable due to the very limited availability of the measurements. The parameter A describes the specific grid cell area. For the heat capacity h we apply a constant value of 18,000 Jg^{-1}, which represents an average of experimentally found heat capacity values [e.g., *Dickinson and Kirkpatrick*, 1985; *Reid and Robertson*, 2012, and references therein] that are widely used in fire spread models [e.g., *Andrews*, 2009; *Thonicke et al.*, 2010]. Note that the FRP values calculated by equation (1) represent the mean daily fire radiative energy that is emitted from all fires burning in a grid box within 24 h. For evaluation of the model the FRP can be compared to assimilated mean daily FRP values in the Global Fire Assimilation System (GFAS), a satellite-based FRP and emission data set [*Kaiser et al.*, 2012].

Due to the fact that emission heights need to be calculated for individual fires rather than for a mean fire state of a grid box, FRP, and emissions, which are only provided as grid box means by JSBACH-SPITFIRE, have to be distributed to individual fires. Therefore, we implement a statistical-empirical distribution function which is based on global mean FRP distributions for single fires in the GFASv1.2 data set. A more detailed description of the FRP distribution scheme, which we implemented in JSBACH-SPITFIRE, is provided by Appendix A. An evaluation of the normalized JSBACH-SPITFIRE FRP distribution for PD climate conditions against GFAS is provided in the results section.

The fraction of carbon emitted as black carbon (BC) and organic carbon (OC) is calculated using species-specific wildfire emission factors by *Akagi et al.* [2011]. In contrast to OC, which contributes about 80% to the total aerosol mass emitted from wildfires, BC, contributing only about 10% to the total emitted aerosol mass, is much more absorbing. Therefore, BC is most important for climate change parameters like the aerosol-radiative forcing introduced by wildfires. We also use *Akagi et al.* [2011] emission factors for $\mathrm{SO_2}$ except for extratropical forests, which are not specified in this reference. For the latter we apply emission factors from *Andreae and Merlet* [2001]. For all emission factors, plant functional types (PFTs) in JSBACH are attributed to land cover types (LCTs) provided by *Akagi et al.* [2011] as shown in Table 1. Due to the dominant radiative forcing and climate impact of BC compared to OC and SO_2 emissions from wildfires [e.g., *Bond et al.*, 2013; *Boucher et al.*, 2013], the analysis provided in the results section of this study is largely limited to future changes in BC emissions and concentrations.

Table 1. Attribution of JSBACH Plant Functional Types (PFTs) to Land Cover Types (LCTs) for Emission Factors described in *Akagi et al.* [2011]

JSBACH PFT	Attributed Akagi LCT
Tropical Evergreen Trees	Tropical Forest
Tropical Deciduous Trees	Tropical Forest / Savanna[a]
Extratropical Evergreen Trees	Extratopical Forest
Extratropical Deciduous Trees	Extratopical Forest
Raingreen Shrubs	Savanna / Chaparral[b]
Deciduous Shrubs	Savanna / Chaparral[b]
C3 Grass	Savanna
C4 Grass	Savanna
C3 Pasture	Pasture / Savanna[c]
C4 Pasture	Pasture / Savanna[c]
C3 and C4 Crops	Crops[d]

[a] According to the definition of Savanna in *Akagi et al.* [2011], the JSBACH PFT Tropical Deciduous Trees is attributed to Akagi Tropical Forest, if the sum of the JSBACH PFTs Tropical Evergreen Trees and Tropical Deciduous Trees is greater than 60%, otherwise it is assigned to the Akagi LCT Savanna.

[b] JSBACH Raingreen Shrubs and Deciduous Shrubs are assigned to the Akagi LCT Savanna in the tropics and the Akagi LCT Chaparral in the extratropics.

[c] JSBACH C3 Pasture and C4 Pasture are assigned to the Akagi LCT pasture only if the Pasture fraction is larger than 50%, otherwise they are attributed to the Akagi LCT Savanna.

[d] Crops in JSBACH are prescribed to be not affected by fires.

All JSBACH-SPITFIRE simulations are run for 1850–2005 as described in *Lasslop et al.* [2014], except that atmospheric forcing was provided by MPI-ESM model output of the model intercomparison project CMIP5 [*Giorgetta et al.*, 2013] and not from reanalysis data. For 2006–2100, MPI-ESM model output for the RCP scenarios RCP2.6, RCP4.5, and RCP8.5 is applied [*van Vuuren et al.*, 2011]. RCPs define greenhouse gas concentration scenarios which lead to a specific radiative forcing in the year 2100, e.g., a radiative forcing of 8.5 W m^{-2} for RCP8.5. Population density for 1850–2005 is prescribed according to the History Database of the Global Environment (HYDE) [*Goldewijk*, 2001; *Klein Goldewijk and Verburg*, 2013] and has been extended for the years 2006–2100 by population density changes predicted from Shared Socioeconomic Pathways (SSPs) relative to HYDE data for 2010. SSP scenarios describe the interaction of climate change scenarios with social, economical, and political changes in terms of mitigation and adaptation. Combinations of SSP and RCP scenarios are chosen according to the suggestions by *van Vuuren and Carter* [2014]: RCP2.6+SSP1, RCP4.5+SSP1, and RCP8.5+SSP3. Land use change is taken from *Hurtt et al.* [2011] as described in *Reick et al.* [2013].

2.2. ECHAM6-HAM2 Model Description

In a second step, we use the global circulation model ECHAM6 extended by the aerosol module HAM2 to simulate atmospheric circulation, aerosol microphysics, and radiation. ECHAM6, the atmospheric component of MPI-ESM [*Giorgetta et al.*, 2013; *Stevens et al.*, 2013], is run at a horizontal resolution of approximately 1.9° × 1.9° with 47 vertical layers from the surface up to 0.01 hPa; a time step of 10 min is applied. For the RCP scenarios 2090–2099 sea surface temperature (SST) is prescribed according to MPI-ESM CMIP5 simulations, whereas for PD simulations, it is prescribed according to the Atmospheric Model Intercomparison Project (AMIP) [*Hurrell et al.*, 2008]. The aerosol component HAM2 [*Stier et al.*, 2005; *Zhang et al.*, 2012] models the transport and removal of trace gas and aerosol species including, among others, BC, OC, and SO_2, which represent the major wildfire emission species. Aerosol emissions are thereby prescribed as boundary conditions. By use of Mie theory, aerosol optical properties are calculated for 24 solar spectral bands and serve as input for the ECHAM6 radiation scheme. In addition, a two-moment cloud microphysics scheme [*Lohmann et al.*, 2007] coupled to the aerosol microphysics enables the simulation of aerosol-cloud interactions. Because of the internal mixing of aerosol particles by the microphysics module M7, the AOT calculated by the model represents an integrated AOT including contributions of BC, OC, and SO_2. The calculation of the individual AOT contributions by the individual aerosol species would require completely separate model runs. These computationally expensive ECHAM6-HAM2 simulations go beyond the scope of this study which focuses on the potential overall aerosol-climate impact of future changes in wildfire activity.

2.3. Wildfire Emission Heights

For consistency with previous studies, the term “wildfire emission heights” in this study describes the full range of heights above surface at which emissions are injected into the atmosphere [see *Veira et al.*, 2015a]. Maximum emission heights in ECHAM6-HAM2, also referred to as “top plume heights,” are simulated by a semiempirical plume height parametrization, which is based on the parameters FRP (P_f), Brunt-Väisälä frequency of the atmosphere (N), and planetary boundary layer (PBL) height (H_{PBL}). Originally developed by *Sofiev et al.* [2012], we apply the ECHAM6-HAM2 specific modifications presented by *Veira et al.* [2015b] including a tuning of FRP for high plumes and the introduction of a diurnal cycle in FRP. Top plume heights (H_p) are simulated as follows:

$$H_p = \alpha H_{\mathrm{PBL}} + \beta \left(\frac{P_f}{P_{f0}} \right)^{\gamma} \exp\left(-\delta N^2 / N_0^2\right) \tag{2}$$

whereupon

$$P_f = \begin{cases} P_f & \text{if } H_p \leq 1500\mathrm{m} \\ P_f \times \left(\frac{H_p}{1500\,\mathrm{m}} \right)^{0.5} & \text{if } H_p > 1500\,\mathrm{m}. \end{cases} \tag{3}$$

The reference Brunt-Väisälä Frequency (N_0) and the reference FRP (P_{f0}) hold fixed values of $N_0 = \sqrt{2.5 \times 10^{-4}\, s^{-1}}$ and $P_{f0} = 10^6$ W, respectively. The constant values of α, β, γ, and δ have been determined by use of a computational learning data set; for more detailed information see *Sofiev et al.* [2012]. We distribute all wildfire emissions vertically with constant mass mixing ratio from the top of the plume to the surface.

2.4. Emission Inventories

Wildfire emissions in our ECHAM6-HAM2 simulations are either based on JSBACH-SPITFIRE emissions for PD climate conditions (1996–2005) or JSBACH-SPITFIRE RCP scenarios for 2090–2099. SPITFIRE emissions have been tuned against the Global Fire Emissions Database (GFED) [*van der Werf et al.*, 2010], which are known to result in a global underestimation of AOT [e.g., *Chin et al.*, 2009; *Matichuk et al.*, 2008; *Tosca et al.*, 2010]. Therefore, we apply a zero-order emission correction factor of 3.4 for wildfire emissions as described in *Huijnen et al.* [2012], *Kaiser et al.* [2012], and *von Hardenberg et al.* [2012] for all simulations. There is evidence for a strong underestimation of BC and OC aerosol emissions in all bottom-up fire emission inventories. These biases might partly be related to the strong uncertainties in the estimation of the biomass burned, but there are several other major sources of model uncertainties including the application of species-specific emission factors and the model specific parametrizations of wet and dry deposition rates [e.g., *Kaiser et al.*, 2012; *Schwarz et al.*, 2013]. *Zhang et al.* [2014] applied 12 different state-of-the-art biomass burning emission inventories in a regional modeling study and found that for February 2012 in sub-Saharan Africa the mean monthly emission estimates of the various inventories differed up to a factor of 12 and introduced differences in the AOT of up to a factor of 7. The studies mentioned above provide a rough estimation of the uncertainty ranges in the emission inventories as such and also of their impacts on atmospheric parameters, which also apply to this study.

In addition, we run one simulation with prescribed FRP and emissions from the GFASv1.2 data set. While the FRP simulated by JSBACH-SPITFIRE is directly comparable to the assimilated GFAS FRP, the emission fluxes in GFAS apply geographical PFT distributions and emissions factors, which show distinct differences compared to the JSBACH-SPITFIRE model. Therefore, the simulated JSBACH-SPITFIRE emission fluxes cannot be expected to perfectly match the satellite-based GFAS emissions. However, the differences between the ECHAM6-HAM2 simulation with prescribed GFAS emissions and the ECHAM6-HAM2 simulation with JSBACH-SPITFIRE emissions provide valuable estimates, how differences in the emission inventories impact atmospheric parameters like BC concentrations and AOT.

Anthropogenic and biogenic emissions are taken according to the HAM2.2 standard setup using AEROCOM phase II emissions for all simulations [*Stier et al.*, 2005; *Dentener et al.*, 2006]. These represent PD emission inventories. To estimate the relative importance of changes in wildfire emissions compared to future changes in anthropogenic emissions, we also apply projected changes in anthropogenic emissions according to RCP8.5 [*Lamarque et al.*, 2011] for one simulation. Sea salt, marine Dimethyl Sulfide (DMS), and dust emissions in ECHAM6-HAM2 are calculated interactively based on surface wind speed and hydrological parameters, respectively [*Stier et al.*, 2005; *Zhang et al.*, 2012, and references therein].

Table 2. Setup of ECHAM6-HAM2 Experiments[a]

Simulation Name	Time Period	Climate Scenario	Anthropogenic Emissions	Wildfire Emissions and FRP
RCP2.6-SPITFIRE	2090–2099	RCP2.6	AEROCOM 2000	SPITFIRE RCP2.6
RCP4.5-SPITFIRE	2090–2099	RCP4.5	AEROCOM 2000	SPITFIRE RCP4.5
RCP8.5-SPITFIRE	2090–2099	RCP8.5	AEROCOM 2000	SPITFIRE RCP8.5
PD-SPITFIRE	1996–2005	AMIP	AEROCOM 2000	SPITFIRE PD
CLIMATE-ONLY	2090–2099	RCP8.5	AEROCOM 2000	SPITFIRE PD
RCP8.5-SPITFIRE+ ACCMIP-2090	2090–2099	RCP8.5	ACCMIP RCP8.5 2090	SPITFIRE RCP8.5
PD-GFAS	2003–2011	AMIP	AEROCOM 2000	GFASv1.2 2003–2013

[a] All SPITFIRE simulations and the CLIMATE-ONLY experiment use wildfire emissions from JSBACH-SPITFIRE output. Simulation "PD-GFAS" employs wildfire emissions from the Global Fire Assimilation System (GFAS) for the period 2003–2011. Emission heights are calculated by a modified version of the Sofiev plume height parametrization [*Veira et al.*, 2015b]. See text sections 2.3 to 2.5 for more detailed information.

2.5. Scenario Setup

We run three JSBACH-SPITFIRE simulations for the scenarios RCP2.6, RCP4.5, and RCP8.5. These simulations provide the wildfire emission and FRP input for the ECHAM6-HAM2 simulations. All scenarios are carried out for the time period 1850–2100 as described in section 2.1. The vegetation carbon pools are run into equilibrium prior to 1850 realized by a spin-up of 300 years. The model spin-up equilibrates the fast carbon pools, whereas slow soil carbon pools are not considered and do not interact with fires.

The setup of the ECHAM6-HAM2 simulations is described in Table 2. The ECHAM6-HAM2 experiments RCP2.6-SPITFIRE, RCP4.5-SPITFIRE, and RCP8.5-SPITFIRE are run for the period 2090–2099. They combine the change in wildfire emissions, FRP, and projected changes in climate, which impact emission heights, dust, DMS and sea salt mobilization, aerosol transport, and aerosol removal rates. Compared to simulation PD-SPITFIRE, which represents PD wildfire emissions and climate, these simulations demonstrate the potential effects of climate-induced changes in wildfire emissions on atmospheric aerosol concentrations in a warmer climate at the end of the 21st century. In experiment CLIMATE-ONLY, PD SPITFIRE emission fluxes are applied together with future climate conditions from the RCP8.5 scenario. The comparison of simulation CLIMATE-ONLY to simulation RCP8.5-SPITFIRE enables us to disentangle the combined impact of changes in FRP, emission fluxes, and emission heights from changes caused by altered atmospheric conditions alone.

Simulation RCP8.5-SPITFIRE+ACCMIP-2090 is identical to RCP8.5-SPITFIRE except for the anthropogenic emissions which represent projected future RCP8.5 emissions of the year 2090 [*Lamarque et al.*, 2011]. These anthropogenic ACCMIP BC and OC emission projections for the year 2090 are only 47% and 61%, respectively, of the PD anthropogenic AEROCOM emissions used in all other simulations. Thus, the comparison between simulation RCP8.5-SPITFIRE+ACCMIP-2090 and RCP8.5-SPITFIRE provides an estimate of how the relative wildfire contribution to the overall aerosol concentrations might change in the future due to changes in anthropogenic aerosol emissions.

The last simulation called PD-GFAS applies the wildfire emission inventory reported in GFASv1.2 for 2003–2011. It represents a reference simulation for the comparison of JSBACH-SPITFIRE emissions in PD climate conditions to satellite-based emission estimates. Although GFASv1.2 data were available for 2003–2013 at the start of this study, the availability of AMIP SST and sea ice was limited to 2003–2011; therefore, simulation PD-GFAS covers only the period 2003–2011. For all scenarios, one year of ECHAM6-HAM2 model spin-up is run prior to the start year of the simulations.

3. Results

3.1. JSBACH-SPITFIRE Emissions for Present-Day Climate Conditions

The ability of an interactive fire model to realistically simulate global fire activity and fire emissions is largely determined by the process representation of the fire model itself, the general performance of the global vegetation model and the meteorological forcing applied. *Lasslop et al.* [2014] evaluated the JSBACH-SPITFIRE model performance in burned fraction and carbon emissions in detail. The authors found the mean annual carbon emissions of JSBACH-SPITFIRE globally to be 60–70% higher than in GFED3 which lies within the range of the large uncertainties related to satellite-based emission inventories (see section 2.4). Here we focus on the evaluation of simulated emission fluxes of BC, OC, and SO_2 and FRP against satellite-based emission and

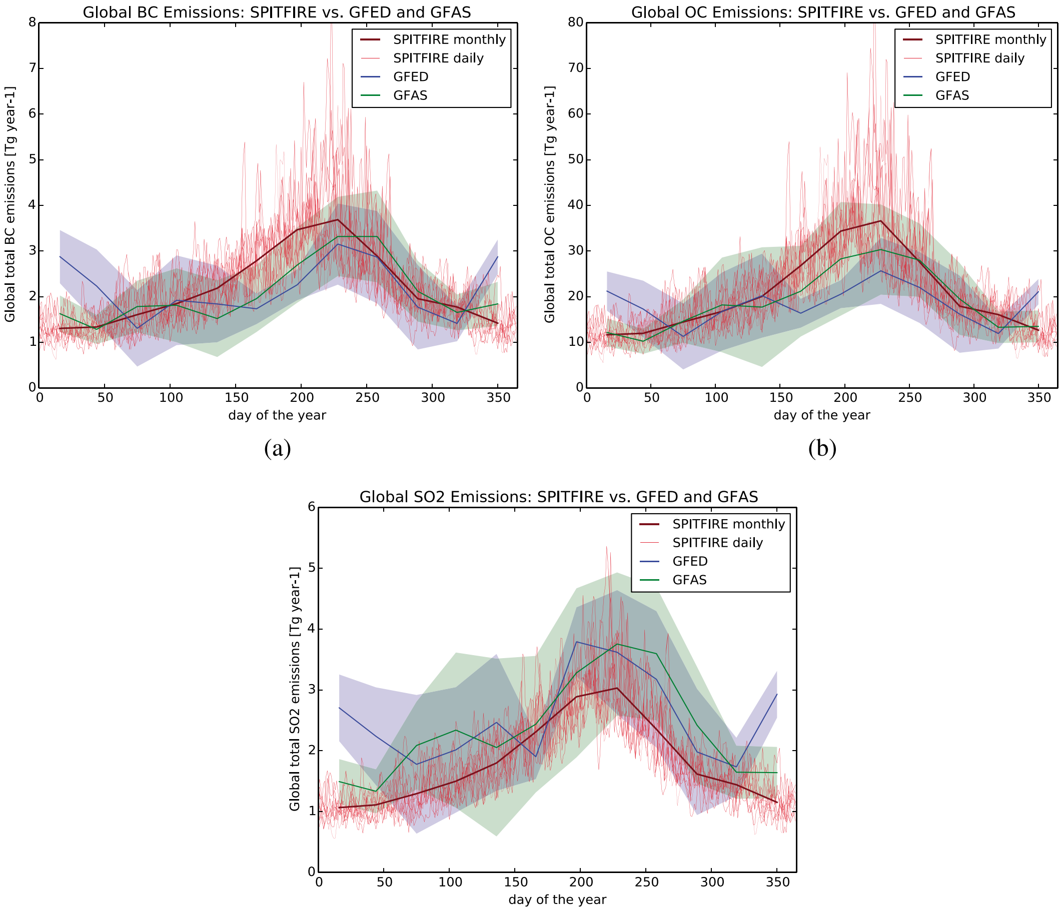

(a) (b)

(c)

Figure 1. Global mean emission fluxes of (a) BC, (b) OC, and (c) SO_2 from wildfires simulated by JSBACH-SPITFIRE for the years 1996–2005 compared to multiyear monthly means of the satellite-based emission inventories GFED and GFAS. Blue and green shadings represent one standard deviation of multiyear monthly means in the observational data sets.

FRP inventories. Figure 1 illustrates a comparison of the mean global total wildfire emission release simulated by JSBACH-SPITFIRE to the emission inventories GFASv1.2 (2003–2013) and GFEDv2 (1997–2008). The global total wildfire BC emissions simulated by JSBACH-SPITFIRE for the years 1996–2005 lie approximately 5% above the satellite-based emission inventories GFED and GFAS. For OC, the JSBACH-SPITFIRE emission estimates are 13% and 8% larger than GFED and GFAS, respectively; for SO_2 negative discrepancies of −28% and −23% are found. The species-specific direction of discrepancies between JSBACH-SPITFIRE and the satellite-based emission inventories can primarily be explained by the application of different emission factor data sets [*Andreae and Merlet*, 2001; *Akagi et al.*, 2011] and differences in the PFT distributions. The seasonality is only partly captured by the model with a slightly too early onset of the Northern Hemispheric fire season. The large differences in emission flux estimates between GFED and GFAS in January and February, however, depict the large uncertainties which are included in both emission inventories. Previous studies [e.g., *Petrenko et al.*, 2012; *Kaiser et al.*, 2012; *Veira et al.*, 2015a] demonstrated that there are strong regional differences in the performance of both data sets due to their dependence on the accuracy of the satellite measurements of burned area (GFED) and FRP (GFAS) which mainly determine the emission estimates. Overall, the differences between the simulated emission estimates and GFAS and GFED lie within the range of the natural interannual variations indicating a reasonable global model performance of JSBACH-SPITFIRE. Therefore, our comparison demonstrates the basic ability of the JSBACH-SPITFIRE model to simulate the global magnitude and seasonal cycle of wildfire emissions for present-day climate.

General region-specific discrepancies in wildfire emission estimates between implementations of SPITFIRE in DGVMs and the satellite-based GFED data set have also been identified in previous studies. *Yue et al.* [2014]

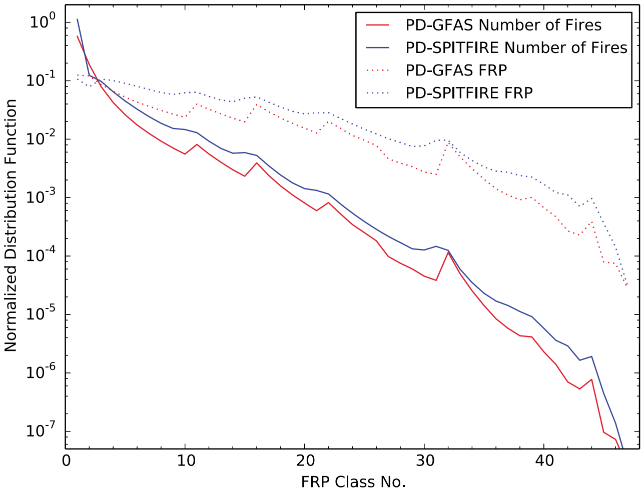

Figure 2. Global mean attribution of normalized FRP and number of fire distributions to FRP classes. Blue lines represent simulated JSBACH-SPITFIRE distributions (1996–2005) and red lines show observational GFAS data (2003–2013). For a description of the FRP class scheme, see Table A1 in Appendix A, respectively, *Veira et al.* [2015b].

implemented the SPITFIRE model into the global vegetation model ORCHIDEE. The authors found similar regional bias patterns in SPITFIRE burned area and wildfire emission fluxes compared to GFED. Nevertheless, other satellite-based data sets (e.g., L3JRC and GLOBCARBON) provide burned area estimates, which show significantly better agreement to SPITFIRE, e.g., in North America [*Yue et al.*, 2015]. For Central Africa, *Zhang et al.* [2014] analyzed eight different satellite-based emission estimates and found large variations between the observational data sets of up to a factor of 10. These regional differences are even larger than most of the regional biases we detect when comparing JSBACH-SPITFIRE to GFAS and GFED. Therefore, the differences between JSBACH-SPITFIRE and GFAS/GFED should not be interpreted as biases in a strict sense rather than indications for large regional uncertainties in FRP estimates.

3.2. JSBACH-SPITFIRE FRP Simulated for Present-Day Climate Conditions

As described in section 2.1, only the daily mean total FRP of a grid cell is calculated by the JSBACH-SPITFIRE model. The distribution of the total FRP to individual fires is realized by an empirical-statistical distribution scheme which is described in more detail in Appendix A. Figure 2 shows a comparison of the number of fires and individual FRP values simulated by the empirical FRP distribution scheme applied in the JSBACH-SPITFIRE simulations to assimilated observational data from GFAS. The specific FRP values of the FRP class numbers 1–47 shown in Figure 2 are provided by Table A1.

Although the transitions between FRP bins with different widths are slightly smoothed out by the empirical distribution scheme, the JSBACH-SPITFIRE FRP spectrum follows the basic shape of the observational GFAS FRP distribution. Taking into account, the large measurement uncertainties included in GFAS, the model describes a reasonable distribution of FRP to individual FRP classes.

The global mean FRP simulated by JSBACH-SPITFIRE (1996–2005) is approximately 47% higher than the GFAS global average for 2003–2013. This discrepancy may potentially relate to the fact that JSBACH-SPITFIRE simulates a large number of small fires, which is not included in GFAS, because fires with FRP values <10 MW are inadequately captured by MODIS FRP measurements [*Roberts et al.*, 2005]. Moreover, the fixed α value (see equation (1)) applied in this study might overestimate the fraction of energy which is emitted as radiation by the fire. Furthermore, also the assumption that the entire fuel of the fuel classes 1–100 h contributes equally to the emitted FRP might enhance the found discrepancies of the global mean FRP values.

However, Figure 3 demonstrates that regionally, the modeled FRP shows substantial differences to the GFAS FRP patterns of up to three magnitudes. These differences are most pronounced in Central North America and Australia. Most likely these bias patterns can be primarily attributed to an overestimation in the modeled JSBACH net primary productivity and the available fuel in these regions [*Lasslop et al.*, 2014]. In Alaska and Northern Eurasia, emission fluxes and FRP might presumably be underestimated by SPITFIRE because of the missing representation of landscape fragmentation, fuel patterns, and the landscape slope in the model

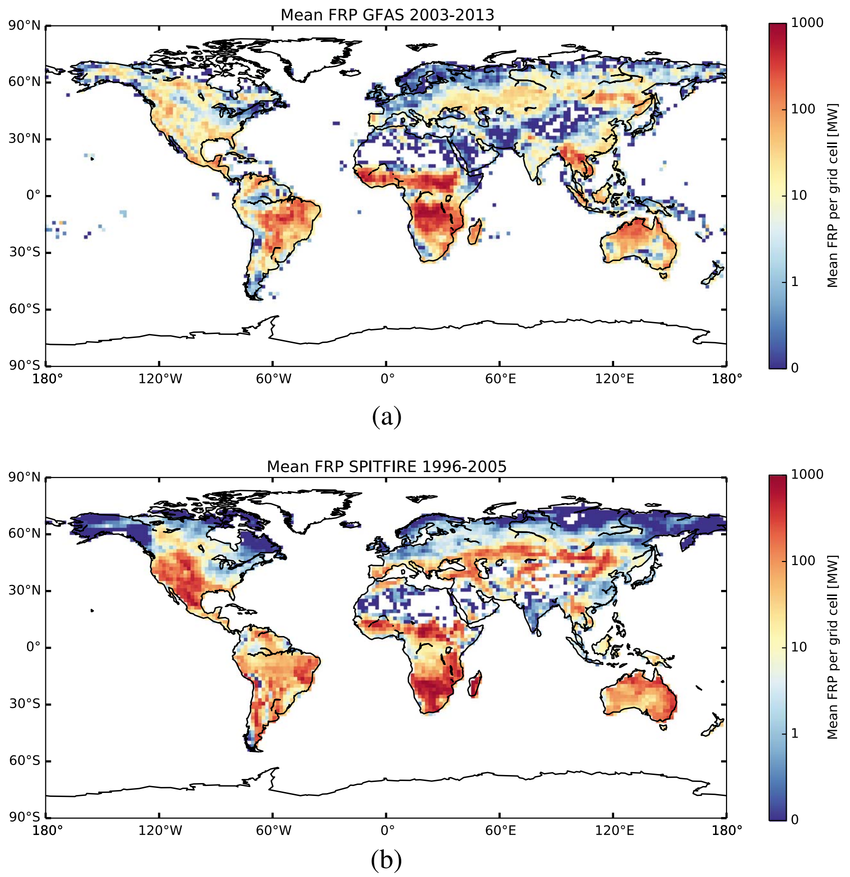

Figure 3. (a) Mean annual FRP per grid cell in the observational GFAS data set 2003–2013 and (b) simulated by JSBACH-SPITFIRE for 1996–2005.

[*Lasslop et al.*, 2014]. Potentially, a replacement of the globally fixed dependency of the human ignition frequency by a region- or landscape fragmentation-specific ignition frequency could improve the model performance in future versions of JSBACÂH-SPITFIRE. However, the FRP patterns of the SPITFIRE model version applied in this study show already good agreement to GFAS in large parts of the tropics which represent the major source regions of wildfire emissions globally.

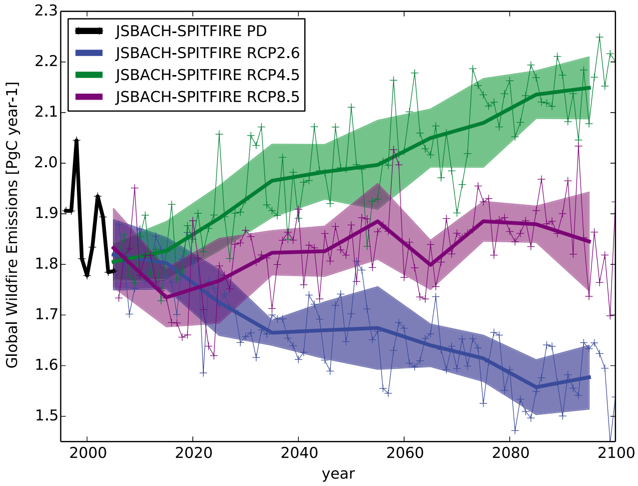

Figure 4. Time series of total C emissions simulated by JSBACH-SPITFIRE for PD and RCP scenarios RCP2.6, RCP4.5, and RCP8.5. Thick solid lines represent decadal means, shadings represent one standard deviation of decadal means. Thin lines show individual yearly means.

While several previous studies have evaluated the JSBACH-SPITFIRE model performance regarding the emission release (see section 3.1), to our knowledge this is the first study which provides FRP estimates from a process-based global fire model.

3.3. Changes in JSBACH-SPITFIRE Emissions Over the 21st Century

Simulated changes in wildfire activity within the 21st century are driven by the complex interaction of human activity, climate change, and changes in vegetation cover. A time series of the total global wildfire carbon emissions simulated by JSBACH-SPITFIRE between 1996 and 2100 is provided by

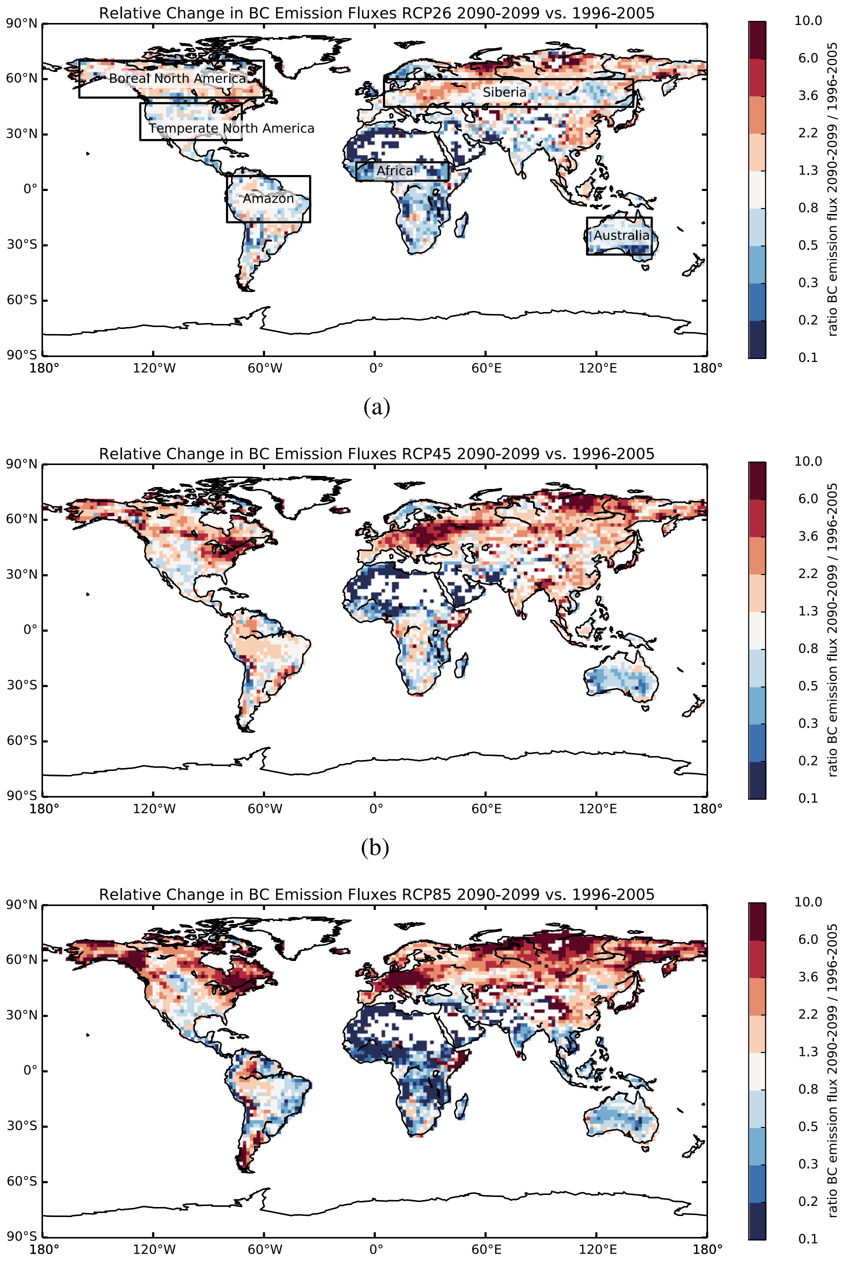

(a)

(b)

(c)

Figure 5. Relative changes in BC emission fluxes simulated by JSBACH-SPITFIRE for (a) RCP2.6, (b) RCP4.5, and (c) RCP8.5 for 2090–2099. All plots show relative differences to present-day (PD) climate conditions (1996–2005). Red colors indicate an increase in emission fluxes; blue colors indicate a decrease in emission fluxes compared to PD. Black rectangles represent region classifications discussed in section 3.4.

Figure 4. Depending on the RCP scenario applied, the total carbon emissions released by wildfires are simulated either to increase by about 15% (RCP4.5), to decrease by about 15% (RCP2.6) or to stay nearly constant (RCP8.5) at the end of the 21st century compared to present day. To understand the projected changes in future wildfire carbon emissions, a more detailed analysis of the regional modifications is required. This section provides a descriptive summary of the global and regional emission flux changes, while potential drivers of these changes are discussed in more detail in the next section. A comparison of the results to previous studies is provided in section 4.

Table 3. Mean Tropical and Extratropical Wildfire Emission Fluxes for the Emission Species BC, OC, and SO_2[a]

Simulation	PD-SPITFIRE	RCP2.6-SPITFIRE	RCP4.5-SPITFIRE	RCP8.5-SPITFIRE
Tropics BC (Tg yr^{-1})	1.11 ± 0.11	0.78 ± 0.09	0.95 ± 0.08	0.70 ± 0.10
NH Extropics BC (Tg yr^{-1})	0.76 ± 0.12	0.82 ± 0.11	1.09 ± 0.15	1.25 ± 0.15
SH Extropics BC (Tg yr^{-1})	0.32 ± 0.05	0.26 ± 0.03	0.35 ± 0.04	0.36 ± 0.05
Tropics OC (Tg yr^{-1})	9.87 ± 0.97	7.05 ± 0.87	8.24 ± 0.70	6.77 ± 0.93
NH Extropics OC (Tg yr^{-1})	8.05 ± 1.33	8.70 ± 1.24	11.97 ± 1.70	13.68 ± 1.67
SH Extropics OC (Tg yr^{-1})	2.72 ± 0.45	2.21 ± 0.32	2.96 ± 0.39	3.55 ± 0.51
Tropics SO_2 (Tg yr^{-1})	0.93 ± 0.09	0.64 ± 0.08	0.87 ± 0.07	0.45 ± 0.06
NH Extropics SO_2 (Tg yr^{-1})	0.64 ± 0.09	0.71 ± 0.09	1.12 ± 0.15	1.18 ± 0.13
SH Extropics SO_2 (Tg yr^{-1})	0.24 ± 0.04	0.19 ± 0.02	0.28 ± 0.03	0.25 ± 0.03

[a] The tropics represent 24.375°N to 24.375°S. All emission fluxes shown in this table describe emission fluxes simulated by JSBACH-SPITFIRE. For the ECHAM6-HAM2 simulations, these emission fluxes are multiplied by the 3.4 correction factor described in *Kaiser et al.* [2012] and *Veira et al.* [2015a]. Uncertainty estimates represent one standard deviation of annual means.

Figure 5 presents global maps of the relative changes in BC emission fluxes for all RCP scenarios 2090–2099 versus 1996–2005. Anthropogenic BC emissions are kept constant at present-day levels for these three simulations (see Table 2). A general increase in boreal wildfire emissions is simulated for all RCP scenarios, with the magnitude of the increase gradually strengthening from RCP2.6 to RCP8.5. While emissions in Africa are consistently shown to decrease for all RCP scenarios, other tropical and subtropical regions (e.g., the Amazon and South East Asia) show different directions of changes in emission fluxes. Table 3 provides a quantitative summary of mean annual tropical and extratropical wildfire emission fluxes for all RCP scenarios and emission species. The decrease in tropical wildfire BC emission fluxes ranges from −14% for RCP4.5 to −37% for RCP8.5. In contrast, extratropical wildfire emissions stay nearly constant for RCP2.6, while they are increased by +32% for RCP4.5 and +49% for RCP8.5, with only negligible differences between emission species. Due to the fact that the FRP is proportional to the biomass burned and thus to the emissions released by a fire, all changes discussed for wildfire emissions similarly apply to changes in FRP.

Besides the mean annual changes, also the seasonal cycle in wildfire emission fluxes is of importance for the atmospheric long-range transport. Figures 6 and 7 illustrate mean zonal daily relative and absolute changes in BC emission fluxes. Midlatitude and boreal fire seasons are simulated to largely expand by up to 1–3 months for RCP8.5. Furthermore, fire activity significantly tends to shift north in the Northern Hemisphere and south in the Southern Hemisphere for RCP8.5. The absolute increase in the midlatitude and boreal BC emission fluxes, which roughly compensates the decrease in the tropical emission fluxes, indicates that the relative importance of extratropical wildfires compared to tropical wildfires might be significantly enhanced in the future.

In addition to the analysis of the changes in emission fluxes, Figure 8 shows the FRP and number of fires spectrum simulated for all RCP scenarios compared to PD-SPITFIRE. For RCP2.6, FRP and the number of fires decrease by about 5–10% for large parts of the distributions, while these change are less pronounced for RCP4.5. For the RCP8.5 scenario, the fraction of intense fires with FRP $>$ 1000 MW is increased by 10–50% compared to PD conditions. In contrast, the fraction of low FRP fires slightly decreases.

3.4. Potential Drivers of Future Changes in Fire Activity

Although it is not possible to fully disentangle all individual parameters which impact fire activity in our set of simulations, we analyzed four region-specific basic drivers of changes in fire activity: human ignitions, fuel available for burning, Fire Danger Index (FDI), and precipitation. The FDI represents a measure for the severity of a fire and takes into account weather-dependent variables like litter moisture, maximum temperature, and dew point temperature [*Thonicke et al.*, 2010]. The named basic drivers of changes in fire activity are analyzed in six regions of distinct changes in emission fluxes (see Figure 5) by calculating Pearson correlation coefficients between changes in specific parameters and the changes in emission fluxes. In summary, the strongest

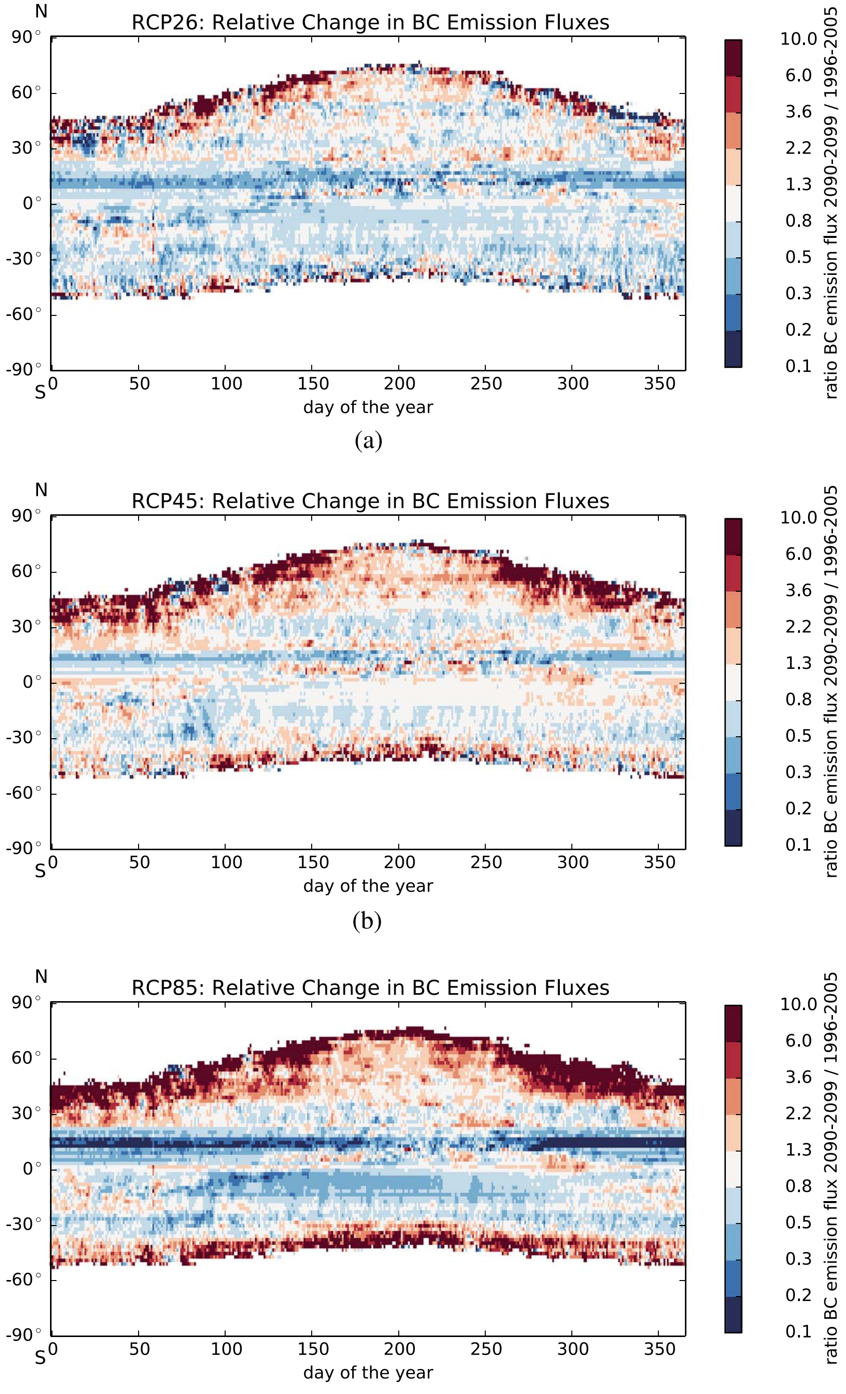

(a)

(b)

(c)

Figure 6. Seasonal cycle of zonal mean relative changes in BC emission fluxes simulated by JSBACH-SPITFIRE for (a) RCP2.6, (b) RCP4.5, and (c) RCP8.5 for 2090–2099. All plots show relative changes to present-day (PD) climate conditions (1996–2005).

correlations can be found between fire emission fluxes and increased precipitation and fuel availability in North America and Siberia. In Africa, a strong decrease in human ignitions due to an increase in population density and land use change represents the driving force for the strong decrease in fire activity. Scenario RCP8.5 shows the largest and most significant correlations, whereas for scenario RCP2.6 and scenario RCP4.5 statistically significant drivers of changes in fire activity could only be found for boreal North America and Africa. The results of our analysis are described in more detail for all regions in Appendix B.

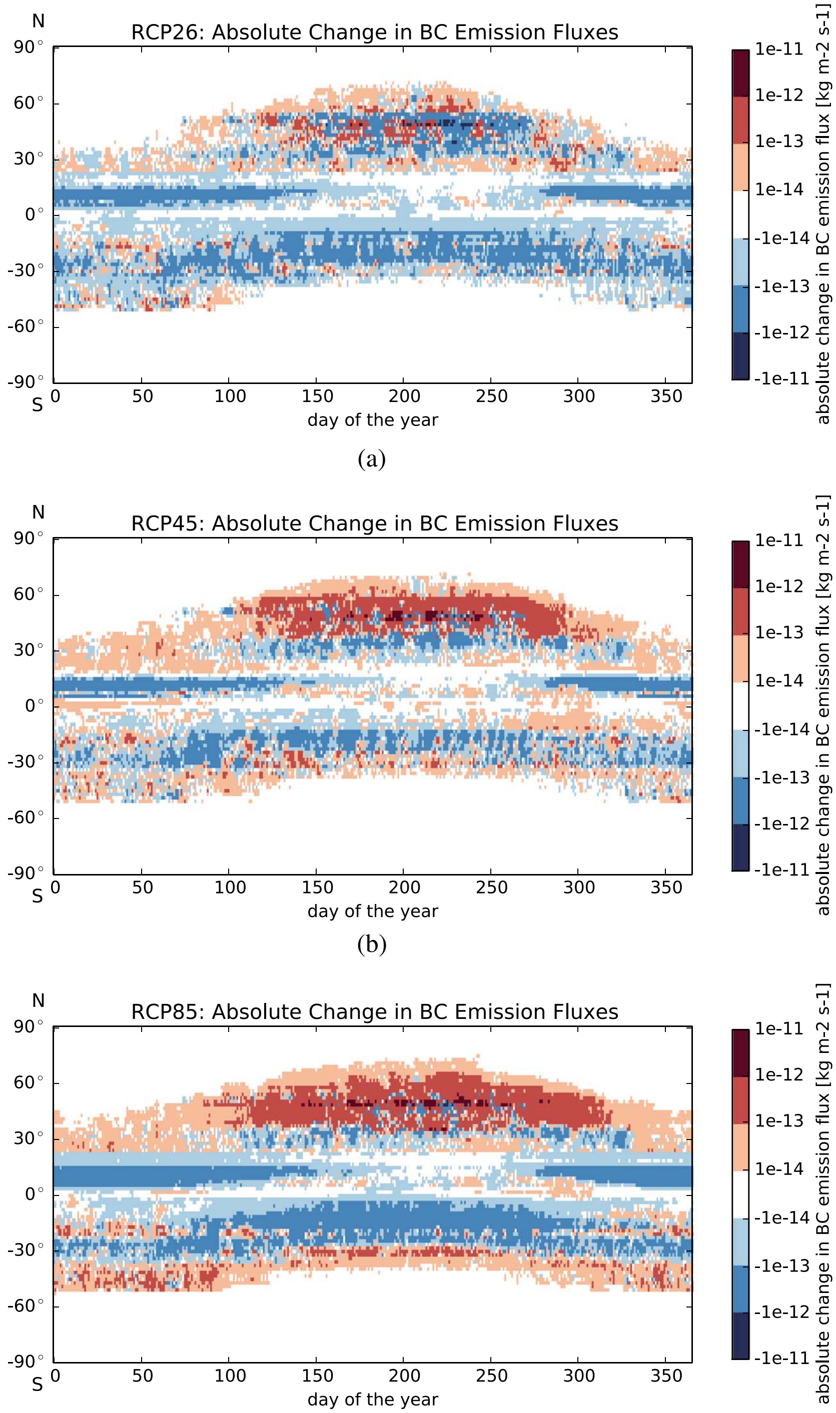

(a)

(b)

(c)

Figure 7. Seasonal cycle of simulated zonal mean absolute changes in BC emission fluxes simulated by JSBACH-SPITFIRE for (a) RCP2.6, (b) RCP4.5, and (c) RCP8.5 for 2090–2099 versus present-day (PD) conditions (1996–2005).

3.5. ECHAM6-HAM2 Emission Heights

While substantial differences in emission fluxes, meteorology, and FRP exist between the RCP scenarios, mean top plume heights in all our simulations show little variation. Between simulation RCP2.6-SPITFIRE featuring the lowest mean plume height (1353 ± 428 m) and PD-SPITFIRE (1640 ± 560 m) featuring the highest mean plume height, a difference of only 300 m is simulated. Figure 9 provides globally averaged plume height distributions for all simulations.

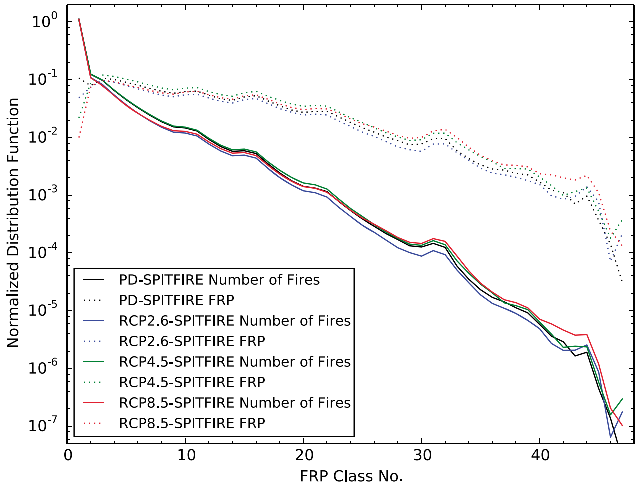

Figure 8. Global mean attribution of normalized FRP and number of fire distributions to FRP classes. Blue, green, and red lines represent JSBACH-SPITFIRE distributions for the RCP scenarios 2.6, 4.5, and 8.5 (years 2090–2099); black lines represent JSBACH-SPITFIRE distributions for PD climate conditions (1996–2005).

Simulation CLIMATE-ONLY represents an RCP8.5 scenario for which wildfire emissions and FRP are kept identical to PD-SPITFIRE, but the meteorology is similar to RCP8.5-SPITFIRE. The largest differences between these simulations are observed for the 99th plume height percentile. Simulation PD-SPITFIRE (3742 m) lies approximately 1.1 km above CLIMATE-ONLY (2686 m) indicating that globally, climate warming entails more stable lower tropospheric conditions which result in lower PBL height and thus tend to dampen plume heights. Due to the fixed fire locations and FRP, global changes in plume heights between simulations PD-SPITFIRE and CLIMATE-ONLY can only be attributed to decreased PBL heights and increased Brunt-Väisälä frequencies (see equation (2)). As no significant changes in Brunt-Väisälä frequencies could be detected (not shown), the observed reduction in plume heights is primarily introduced by an average reduction in PBL heights due to decreased lapse rates. A general decrease in atmospheric lapse rates in a warmer climate and a reduction of PBL heights over land (particularly in the summer season) has also been indicated by several previous studies [e.g., *Joshi et al.*, 2007; *Penrod et al.*, 2014].

The comparison of simulation CLIMATE-ONLY to simulation RCP8.5-SPITFIRE enables us to disentangle the effects of climate change versus changes in FRP on plume heights. With simulation RCP8.5-SPITFIRE showing the highest (3907 m) and CLIMATE-ONLY showing the lowest 99th plume height percentile value (2686 m), we conclude that the increase in FRP overcompensates the climate effect on plume heights for the RCP8.5 scenario and therefore leads to larger plume heights, if both effects are considered. Plume height statistics of simulation RCP8.5-SPITFIRE+ACCMIP-2090 are not shown in Figure 9 as the reduction in anthropogenic emissions compared to simulation RCP8.5-SPITFIRE does not introduce any statistically significant differences. Note that all mean plume heights represent FRP-weighted daily mean plume height values, i.e., fires with high FRP values contribute disproportionately larger to the overall mean. We apply this weighting function to take into account the importance of emission fluxes which linearly scale with FRP (see section 2.1).

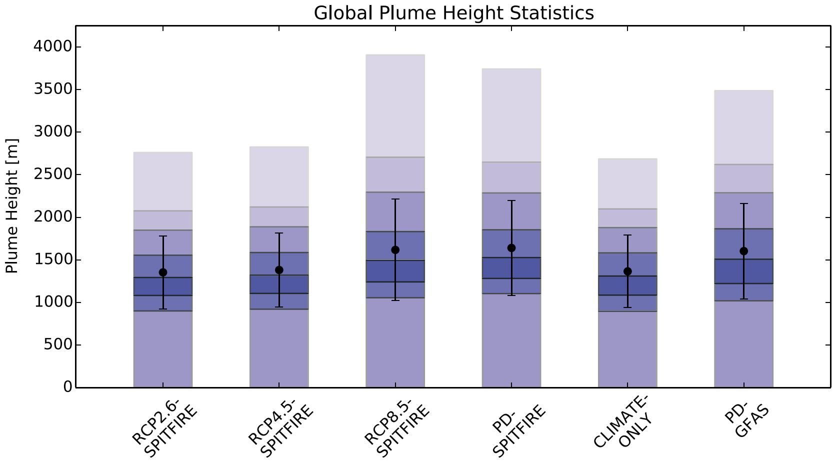

Figure 9. Global plume height statistics for all RCP-SPITFIRE experiments (2090–2099), simulation PD-SPITFIRE (1996–2005), simulation CLIMATE-ONLY (2090–2099), and PD-GFAS (2003–2011). Bluish bars represent 10th, 25th, 50th, 75th, 90th, 95th, and 99th percentiles. Error bars indicate one standard deviation.

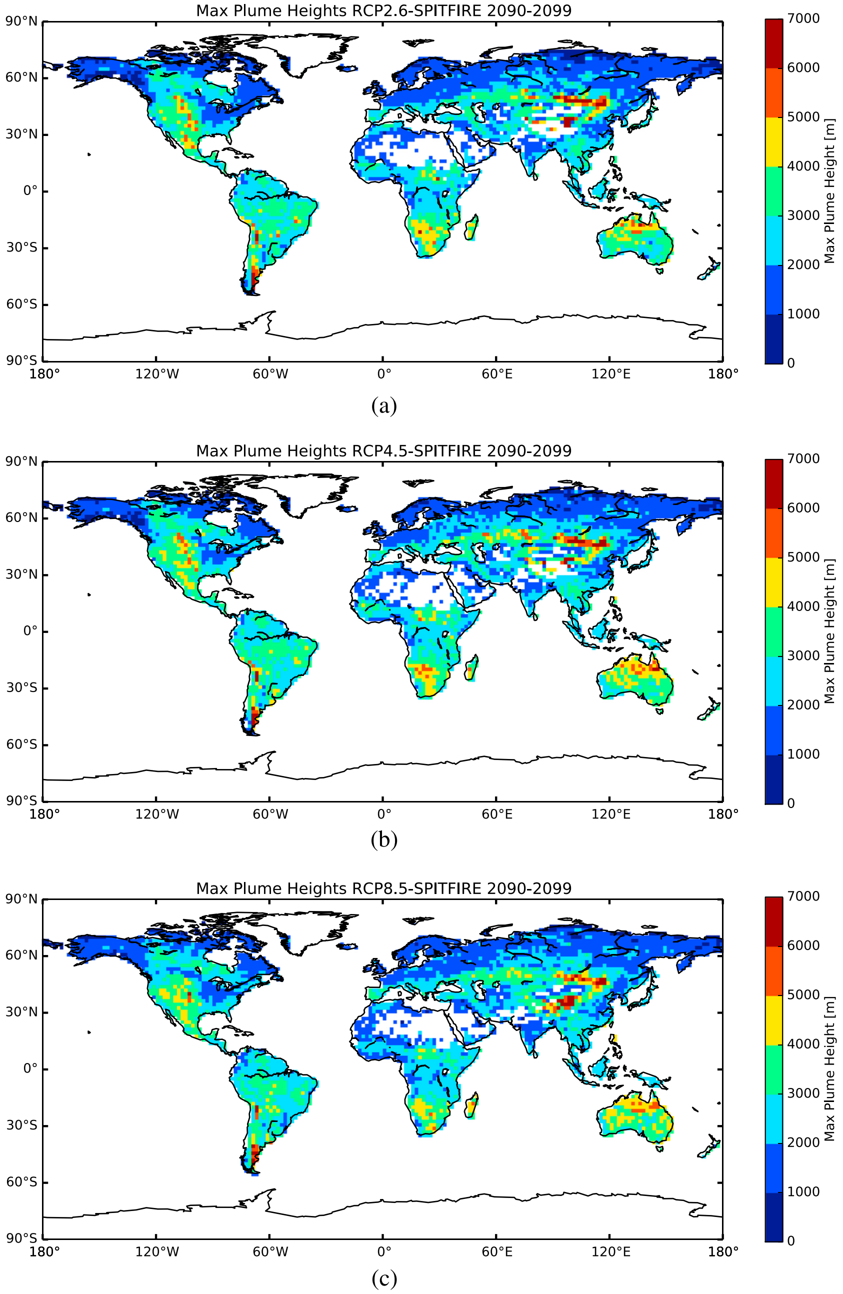

Figure 10. Maximum plume heights of individual fires for (a) RCP2.6-SPITFIRE, (b) RCP4.5-SPITFIRE, (c) RCP8.5-SPITFIRE, (d) PD-SPITFIRE, (e) simulation CLIMATE-ONLY, and (f) simulation PD-GFAS for 2090–2099.

Besides global statistics, the spatial plume height patterns of particularly deep emission injection events are of interest especially for air quality, long-range transport, and removal processes. Figure 10 shows global maps of individual maximum plume heights in the period 2090–2099 for the RCP-SPITFIRE experiments and for simulation PD-SPITFIRE, simulation CLIMATE-ONLY, and simulation PD-GFAS. The general global patterns show differences of less than 1 km in most regions for all six simulations. The increased fire activity in boreal latitudes for simulation RCP4.5-SPITFIRE and RCP8.5-SPITFIRE compared to PD-SPITFIRE causes a slight expansion of maximum plume height >2 km to the north which is not observable for simulation RCP2.6. This northward shift of deep plumes is mainly driven by increased FRP values in these regions. In contrast, plume heights in the Sahel zone are decreased in simulation RCP8.5-SPITFIRE, due to a sharp decline in FRP.

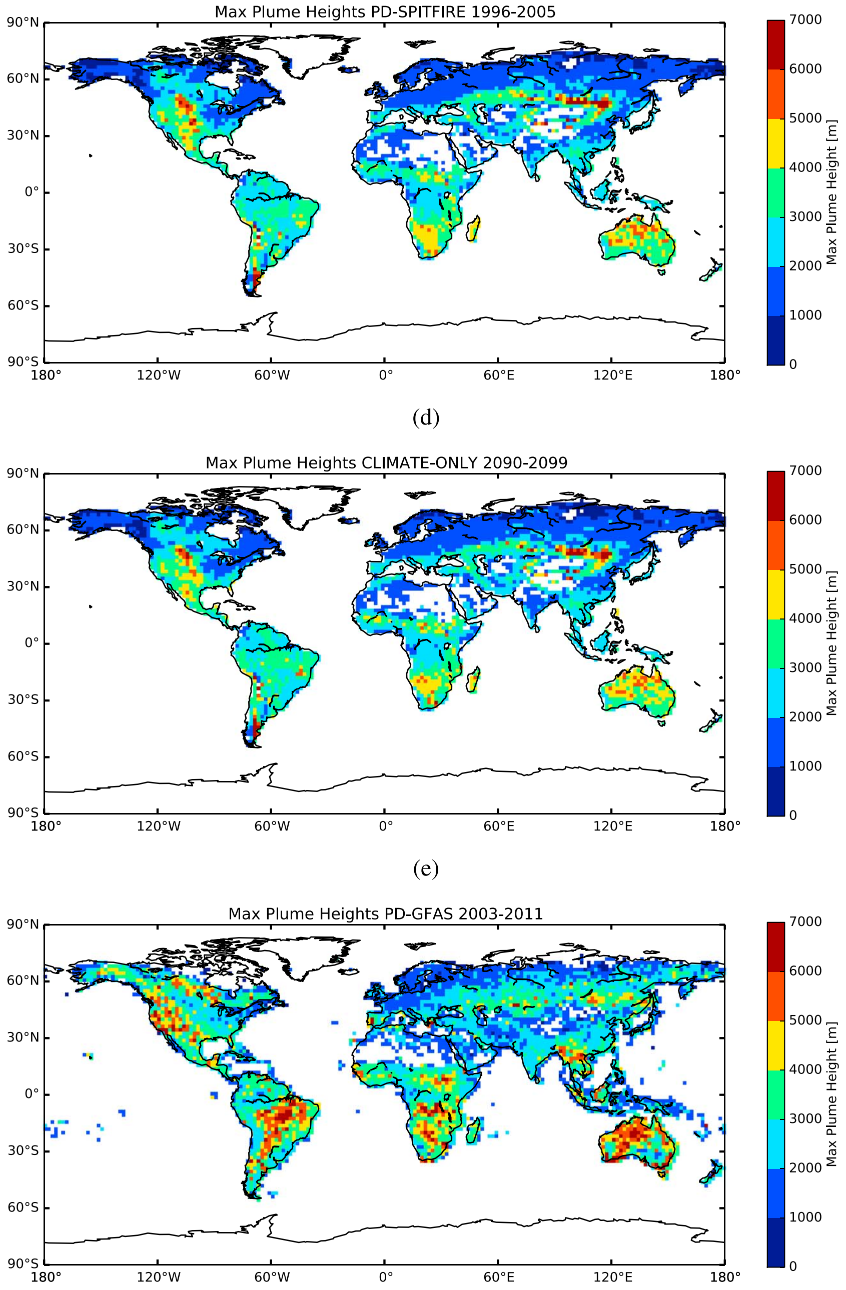

(d)

(e)

(f)

Figure 10. (continued)

The less intense tropical fire activity for the RCP-SPITFIRE scenarios compared to PD conditions is also represented by lower maximum plume heights in central Africa and Northern Australia. Global plume height patterns in simulation CLIMATE-ONLY are very similar to simulation PD-SPITFIRE, but a moderate decrease in tropical plume heights is observable due to more stable atmospheric conditions in the RCP8.5 climate state. The comparison of simulation PD-SPITFIRE to PD-GFAS qualitatively demonstrates the limitations of the model to simulate regional plume height patterns due to biases in fire activity patterns, but it does not represent a detailed validation of the plume height parametrization. Although the global mean plume height statistics show very good agreement for both simulations, the model largely underestimates maximum individual plume heights in Alaska, Northern Siberia, South America, and Australia. Reasonable agreement is achieved

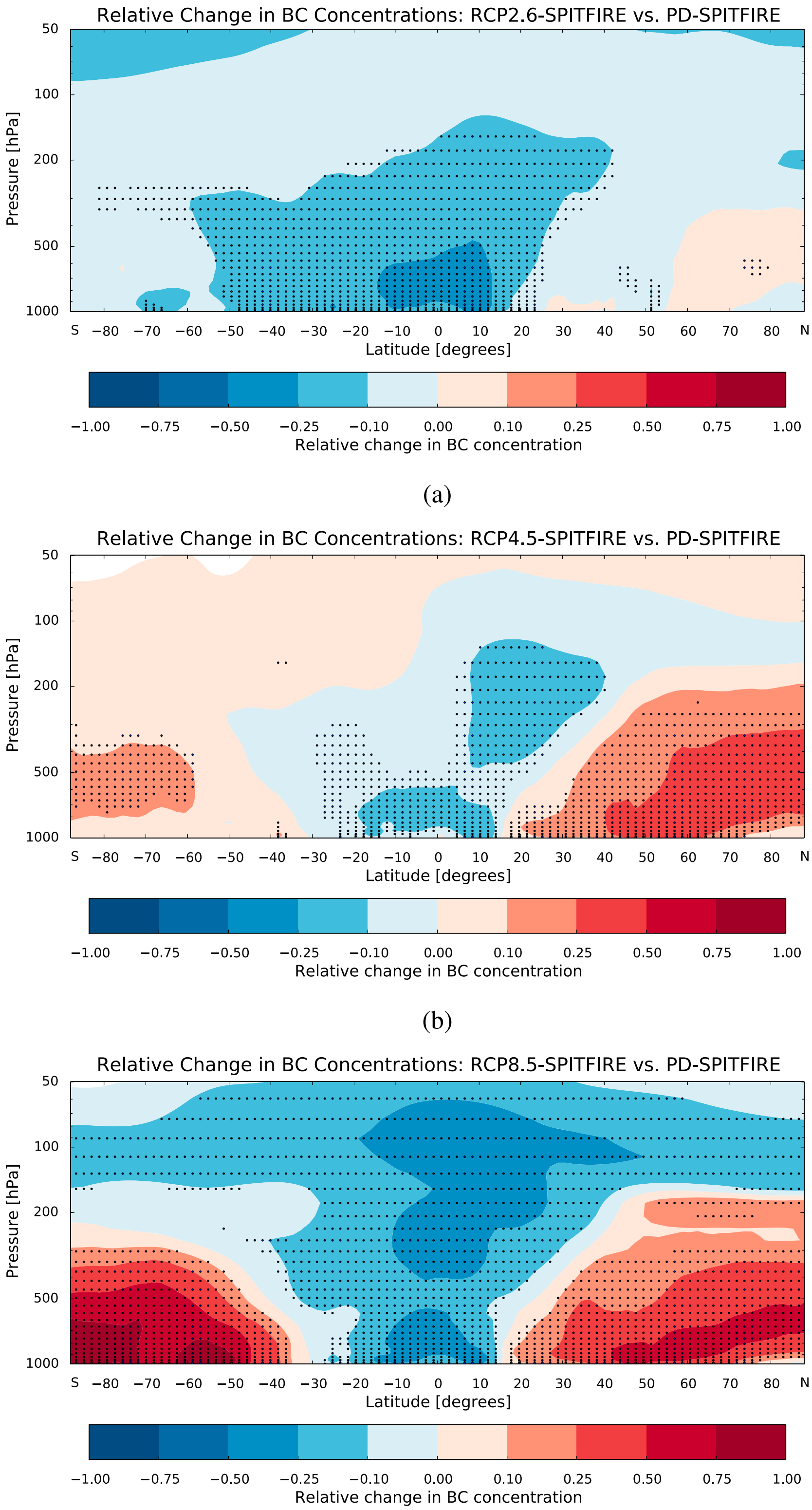
Relative Change in BC Concentrations: RCP2.6-SPITFIRE vs. PD-SPITFIRE

(a)

Relative Change in BC Concentrations: RCP4.5-SPITFIRE vs. PD-SPITFIRE

(b)

Relative Change in BC Concentrations: RCP8.5-SPITFIRE vs. PD-SPITFIRE

(c)

Figure 11. Relative change in mean zonal BC concentrations for (a–c) RCP-SPITFIRE simulations, (d) simulation CLIMATE-ONLY, (e) RCP8.5-SPITFIRE+ACCMIP-2090, and (f) PD-GFAS for 2090–2099; reference simulation is PD-SPITFIRE 1996–2005. Black dots indicate significance based on a student's *t* test at a 95% confidence interval.

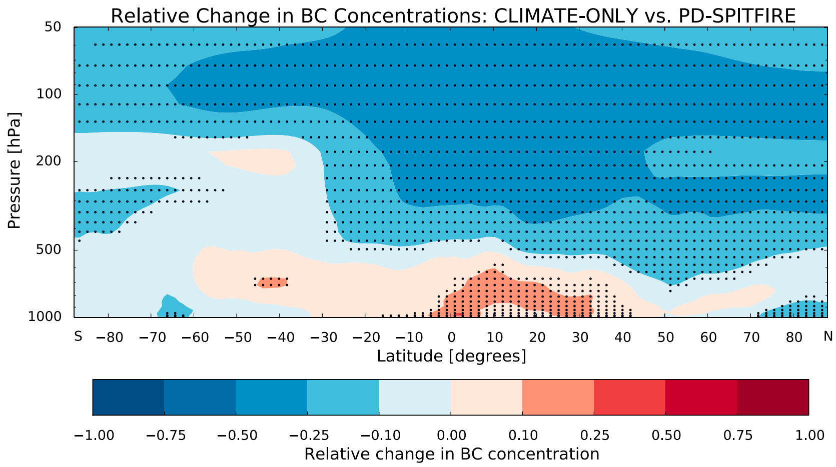

(d)

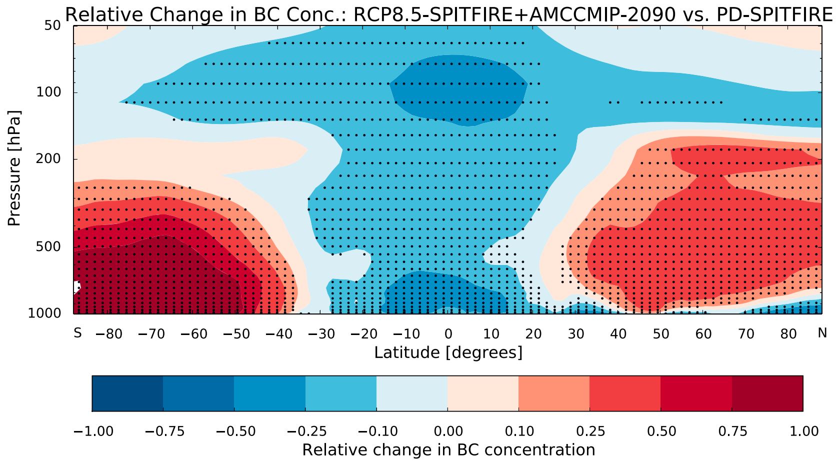

(e)

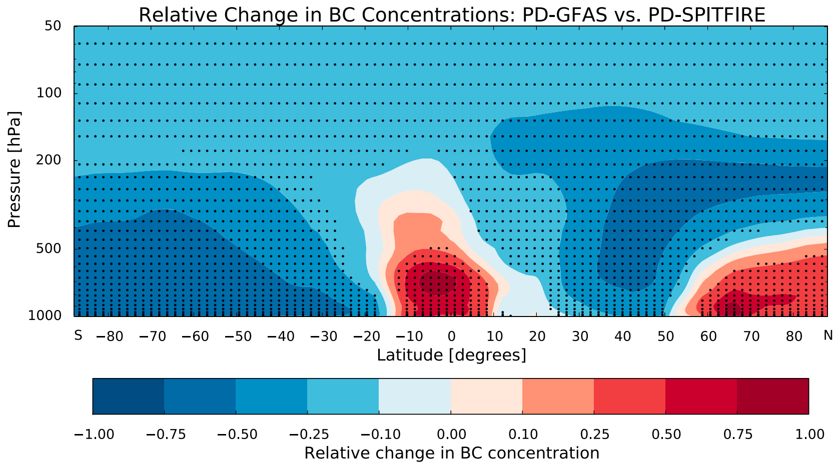

(f)

Figure 11. (continued)

Table 4. Total Removal Rates Represent the Sum of Wet and Dry Deposition and Sedimentation[a]

Simulation	RCP2.6 SPITFIRE	RCP4.5-SPITFIRE	RCP8.5-SPITFIRE	PD-SPITFIRE	CLIMATE-ONLY	RCP8.5-SPITFIRE+ ACCMIP-2090	PD-GFAS
Global removal rates (mg m^{-2} y^{-1})	22.63 ± 0.42	26.15 ± 0.51	25.68 ± 0.89	24.81 ± 0.62	24.81 ± 0.62	20.32 ± 0.86	22.70 ± 3.95
NH Polar removal rates (mg m^{-2} y^{-1})	5.35 ± 0.53	7.21 ± 0.80	8.09 ± 0.93	5.29 ± 0.60	5.85 ± 0.40	7.32 ± 0.74	6.13 ± 1.67
SH Polar removal rates (mg m^{-2} y^{-1})	0.39 ± 0.06	0.47 ± 0.05	0.65 ± 0.08	0.44 ± 0.04	0.46 ± 0.05	0.67 ± 0.07	0.23 ± 0.07

[a] Polar regions represent 67°N–90°N and 67°S to 90°S, respectively. Uncertainty estimates represent one standard deviation of annual means.

for Africa, Europe, and Central Asia. The underestimation of emission fluxes and plume heights in boreal latitudes is presumably related to a poor representation of favorable fire conditions which cause too low FRP values.

3.6. ECHAM6-HAM2 Black Carbon Concentration Profiles

BC concentrations throughout the troposphere are determined by emission fluxes as well as vertical and horizontal transport and removal processes. Figure 11 shows relative differences of mean zonal BC profiles for all simulations shown in Table 2. Lower tropospheric BC concentrations (below 500 hPa) are in all cases clearly related to the regional changes in emission fluxes (see Figure 7). On the other hand, simulation RCP8.5-SPITFIRE clearly demonstrates that upper tropospheric and lower stratospheric BC concentrations are mainly dominated by tropical emission fluxes, because differences in plume heights are negligible and upper tropospheric extratropical BC concentrations decrease even though local emission fluxes are increased (Figure 11c). These findings are consistent with similar aerosol transport mechanisms identified for present-day climate conditions [*Veira et al.*, 2015a].

Figure 11d illustrates that tropical deep convection is generally decreased for RCP8.5 climate conditions leading to a decrease in upper tropospheric BC concentrations by 10–50%, if wildfire emissions are kept constant at PD levels. The impact of changes in emission heights is expected to be small, because in the tropics BC concentrations show a moderate increase between 600 hPa and the surface even though emission heights are decreased in these regions compared to PD conditions. The comparison of simulation RCP8.5-SPITFIRE (Figure 11c) and simulation RCP8.5-SPITFIRE+AMCCMIP-2090 (Figure 11e) indicates that changes in wildfire emissions are of similar importance as the projected reduction (approximately −50%) in BC emissions from anthropogenic sources.

The comparison of simulation PD-GFAS and simulation PD-SPITFIRE (see Figure 11f) provides an estimate, how the differences between a satellite-based emission inventory and the interactively simulated wildfire emissions from JSBACH-SPITFIRE impact atmospheric BC concentrations. While the total global emission fluxes differ by only 5% for present-day climate conditions (see section 3.1), strong regional deviations in

Table 5. Mean AOT Values for 2090–2099 (All RCP Simulations) and 1996–2005 (Simulation PD-SPITFIRE) as Well as 2003–2011 (PD-GFAS)[a]

Simulation	RCP2.6-SPITFIRE	RCP4.5-SPITFIRE	RCP8.5-SPITFIRE	PD-SPITFIRE	CLIMATE-ONLY	RCP8.5-SPITFIRE+ ACCMIP-2090	PD-GFAS
Global mean AOT	0.131 ± 0.002	0.139 ± 0.003	0.151 ± 0.004	0.134 ± 0.002	0.148 ± 0.004	0.136 ± 0.002	0.131 ± 0.006
Tropics mean AOT	0.156 ± 0.004	0.164 ± 0.005	0.179 ± 0.006	0.162 ± 0.003	0.184 ± 0.008	0.165 ± 0.004	0.167 ± 0.009
Extropics NH mean AOT	0.124 ± 0.003	0.136 ± 0.004	0.147 ± 0.005	0.126 ± 0.004	0.116 ± 0.002	0.117 ± 0.004	0.115 ± 0.009
Extropics SH mean AOT	0.104 ± 0.002	0.108 ± 0.002	0.116 ± 0.003	0.104 ± 0.001	0.130 ± 0.004	0.116 ± 0.002	0.098 ± 0.002

[a] Uncertainty estimates represent one standard deviation of annual mean AOT values.

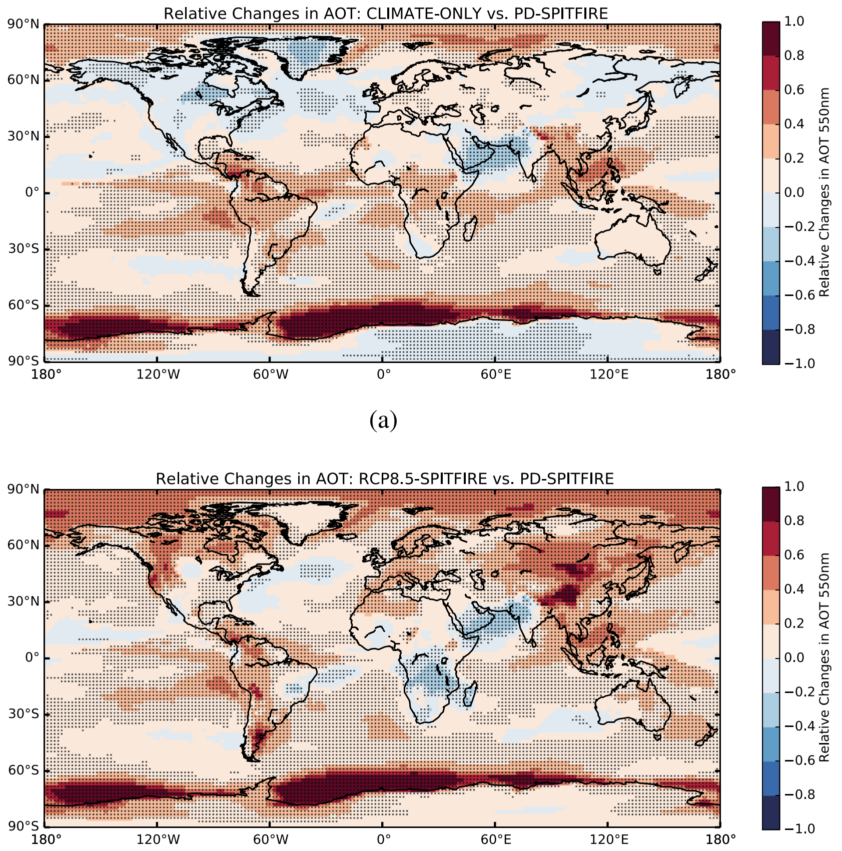

(a)

(b)

Figure 12. Relative changes in AOT@550 nm for simulations (a) CLIMATE-ONLY and (b) RCP8.5-SPITFIRE both representing the time period 2090–2099 compared to the reference simulation PD-SPITFIRE (1996–2005). Black dots indicate significance based on a student's *t* test 95% confidence interval.

atmospheric BC concentrations occur. These regional differences in BC concentrations between simulation PD-SPITFIRE and PD-GFAS show a similar magnitude as the changes from present-day climate conditions to the future RCP climate scenarios. *Veira et al.* [2015a], however, presented comparable regional differences in BC concentrations of up to 50% between GFAS and AEROCOM (based on GFEDv2) emission inventories, which are both satellite-based. Therefore, the presented differences in BC concentrations, which emerge from the choice of the wildfire emission inventory, do not represent model biases in a strict sense, but only provide a rough idea about the uncertainties introduced by the choice of the emission inventory.

Besides BC concentration profiles, BC removal rates in the polar regions might represent a relevant parameter for the overall fire-climate impact, because BC deposition on snow decreases the albedo leading to enhanced melting. A summary of mean annual BC deposition rates is provided in Table 4. Overall changes in future Arctic deposition rates compared to PD-SPITFIRE are small for scenario RCP2.6-SPITFIRE, while a strong increase in BC deposition up to 53% is simulated for RCP8.5-SPITFIRE due to a strong increase in boreal wildfire activity. The comparison of simulation RCP8.5-SPITFIRE to RCP8.5-SPITFIRE+ACCMIP-2090 illustrates that Arctic deposition rates in the RCP8.5 scenarios are largely determined by BC emissions from wildfires, not by anthropogenic emission which are approximately cut by half in the scenario RCP8.5-SPITFIRE+ACCMIP-2090.

3.7. ECHAM6-HAM2 Aerosol Optical Thickness (AOT)

The simulated future changes in AOT at 550 nm are caused by combined changes in aerosol emission fluxes and by changes in atmospheric aerosol processing via transport and aerosol-cloud interactions. Table 5 provides AOT values as global, tropical, and Northern Hemisphere (NH) and Southern Hemisphere (SH) extratropical means for all ECHAM6-HAM2 experiments. While only moderate changes in global AOT are

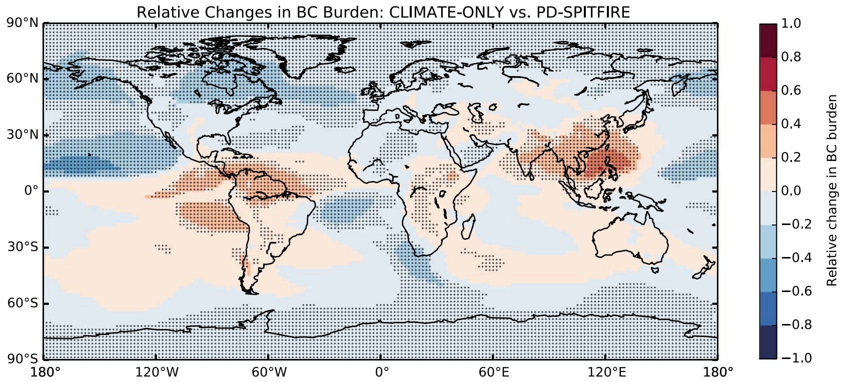

(a)

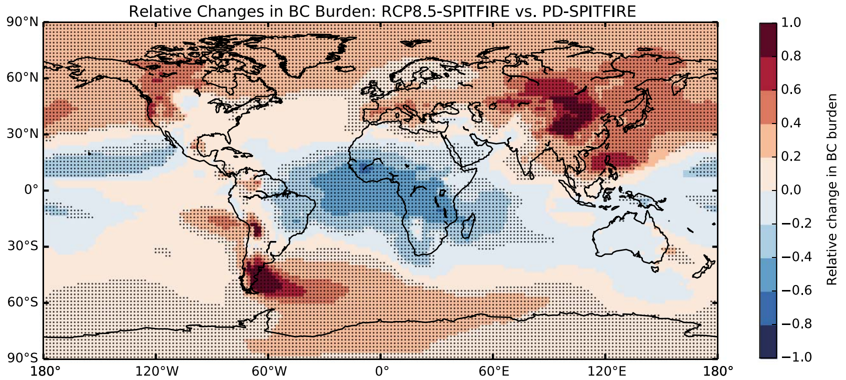

(b)

Figure 13. Relative changes in BC burden for simulations (a) CLIMATE-ONLY and (b) RCP8.5-SPITFIRE both representing the time period 2090–2099 compared to the reference simulation PD-SPITFIRE (1996–2005). Black dots indicate significance based on a student's *t* test at a 95% confidence interval.

simulated for RCP2.6 (0.131 ± 0.002) and RCP4.5 (0.139 ± 0.003) compared to PD-SPITFIRE (0.134 ± 0.002), a considerably stronger increase in AOT is modeled for RCP8.5 (0.151 ± 0.004).

As dust, sea salt and DMS emission fluxes in ECHAM6-HAM2 are calculated interactively and depend on the specific atmospheric conditions, only the comparison of simulation CLIMATE-ONLY to RCP8.5-SPITFIRE enables us to disentangle the particular impact of changes in wildfire emissions from other emission sources. Globally, the significant increase in the AOT for simulation CLIMATE-ONLY compared to PD-SPITFIRE of +10.4 ± 1.1% is induced by the increase in atmospheric dust, sea salt, and DMS burdens of +13.6 ± 5.2%, +7.1 ± 0.8%, and +23.2 ± 0.6%, respectively (see Appendix C for spatial patterns) which are independent from the changes in wildfire emissions. The differences in AOT between simulation CLIMATE-ONLY and simulation RCP8.5-SPITFIRE can primarily be attributed to changes in wildfire emissions. In the extratropical NH, the wildfire-induced increase in AOT for simulation RCP8.5-SPITFIRE (+0.021±0.002) compared to present day (PD-SPITFIRE) is about 2 times larger than the climate change induced reduction in AOT in simulation CLIMATE-ONLY (−0.010 ± 0.001).

Moreover, the modeled total changes in extratropical NH AOT due to changes in wildfire activity are comparable to the projected changes in anthropogenic emissions in the order of −0.030 (see Table 5, RCP8.5-SPITFIRE+ACCMIP-2090). In the tropics, however, the reduction of tropical wildfire emissions in simulation RCP8.5-SPITFIRE compared to simulation CLIMATE-ONLY slightly decreases the mean AOT by −0.005 ± 0.003.

In addition to the globally and zonally averaged AOT values presented in Table 5, Figures 12, and 13 provide global maps of relative changes in AOT and BC burdens for the simulations CLIMATE-ONLY versus PD-SPITFIRE and RCP8.5-SPITFIRE versus PD-SPITFIRE to allow for region-specific analysis of the simulated changes in AOT. In large parts of North America, Asia, and sub-Saharan Africa, distinct changes in BC burdens of −50% to

+100% correspond to AOT changes of similar magnitude for simulation RCP8.5-SPITFIRE (see Figures 12b and 13b, respectively), whereas these regional changes in BC burden and AOT are less pronounced or nonexistent in simulation CLIMATE-ONLY (see Figures 12a and 13a, respectively). Therefore, the simulated changes in wildfire emissions can be identified to represent the major drivers of changes in AOT in these regions of strong wildfire activity. It should be noted that the model setup of our simulations which applies an internal mixing of the aerosols does not allow to disentangle the individual contributions of OC and BC to the total AOT. Results from previous modeling [e.g., *Myhre et al.*, 2009; *Bond et al.*, 2011] as well as observationally based [e.g., *Chung et al.*, 2012] studies, agree that the OC contribution (0.006 to 0.047) to the total AOT is larger than the contribution of BC (0.002 to 0.01) to the total AOT. The top of atmosphere radiative forcing, however, is largely dominated by the BC contribution.

Other region-specific patterns, such as the strong relative increase in AOT around Antarctica and a moderate increase in AOT over large parts of the tropical oceans, are similarly observable in simulation CLIMATE-ONLY and RCP8.5-SPITFIRE. In these regions the BC burdens do not hold comparable changes, and therefore, we conclude that changes in AOT in the polar regions and over the tropical oceans are not primarily caused by changes in wildfire activity, but by changes in dust, sea salt, and DMS emission fluxes (see also Appendix C).

Overall, the changes in wildfire emissions can be identified to represent the major driver in AOT changes only in the vicinity of the main biomass burning regions. It is uncertain, whether a similar AOT impact of changes in wildfire emissions and climate conditions is applicable to the scenarios RCP2.6 and RCP4.5. For a more detailed analysis, further simulations with RCP2.6 and RCP4.5 climate conditions and fixed PD wildfire emissions would be required. But due to the high computational costs, they could not be carried out in the framework of this study.

4. Summary and Conclusions

In this study the process-based global vegetation fire model JSBACH-SPITFIRE [*Lasslop et al.*, 2014] is used to simulate changes in wildfire emission fluxes and FRP during the 21st century. Wildfire emission fluxes and FRP modeled by JSBACH-SPITFIRE are employed to investigate the fate of the wildfire aerosol emissions in the atmosphere using the aerosol-climate model ECHAM6-HAM2 for the period 2090–2099 [*Stier et al.*, 2005; *Zhang et al.*, 2012]. The emission release into the atmosphere in ECHAM6-HAM2 is implemented by a semiempirical plume height parametrization based on FRP from JSBACH-SPITFIRE and atmospheric stability parameters from ECHAM6-HAM2 [*Sofiev et al.*, 2012; *Veira et al.*, 2015b].

The combined set of JSBACH-SPITFIRE and ECHAM6-HAM2 model simulations enables us to quantify not only the projected future changes in wildfire emission fluxes but also to assess the impact of changes in emission heights and emission fluxes on atmospheric BC concentrations and AOT. The major findings of this study can be summarized as follows:

1. The complex interactions of changes in climate conditions, population density, and land use within the 21st century result in diverse, region-specific changes in future wildfire activity. While extratropical fire emissions stay nearly constant for the RCP2.6 scenario in 2090–2099 compared to present-day, substantial enhancements in extratropical emission fluxes of +32% and +48% are simulated for RCP4.5 and RCP8.5. The length of the boreal and temperate fire seasons is enlarged by 1–3 months on average. In the tropics, wildfire emissions are decreased by −14 to −37% for all RCP scenarios.
2. Compared to present-day conditions, a future increase in atmospheric stability generally tends to dampen the mean plume heights by about −0.3 km and the 99th percentile by approximately −1.1 km for RCP8.5. An increase of similar magnitude in the mean plume heights and in the 99th percentile of +0.3 km and +1.2 km is introduced by a significant intensification of strong fires in RCP8.5. For RCP2.6 and RCP4.5 plume heights are reduced primarily due to the combined increase in atmospheric stability and decreased or constant fire intensities. If the wildfire emission release is prescribed at the surface for present day and future climate, the increase in atmospheric stability would introduce a slightly decreasing trend in atmospheric BC long-range transport of the wildfire emissions.
3. Lower tropospheric BC concentrations basically demonstrate the response to the regional changes in wildfire emission fluxes. Upper tropospheric BC concentrations, however, are mainly determined by tropical convection with little influence of the emission heights.
4. Our results for the RCP8.5 scenario demonstrate that the changes in wildfire emissions may largely compensate the projected reduction in anthropogenic BC emissions by the end of the 21st century.

5. For the strongest warming scenario RCP8.5, a significant increase in AOT of +0.031 ± 0.002 is introduced by the changes in wildfire emissions for the Northern Hemispheric extratropics. Globally, however, the mean increase in AOT is small (+0.003 ± 0.002) because of the substantial decrease in tropical wildfire activity.

Although different in its magnitude, a distinct increase in future boreal and midlatitude wildfire activity and a decrease in tropical wildfire activity has been indicated by a large number of previous studies [*Flannigan et al.*, 2009; *Moritz et al.*, 2012, and references therein]. Our results are basically in line with the general findings of those studies but depending on the specific RCP scenario; the magnitude of changes in wildfire emission release shows large regional variations. Fire activity projections by *Pechony and Shindell* [2010] suggested that future fire activity might primarily be driven by temperature change rather than anthropogenic activities. For our JSBACH-SPITFIRE setup only extratropical changes in fire activity are mainly driven by the combined changes in increased fuel availability and more favorable fire conditions, whereas human activities prescribed in this study dominate the changes in tropical fire activity. A recent study by *Knorr et al.* [2015] which further investigates the contributions of climate, CO_2, and demographic impacts on global wildfire emissions basically supports our findings.

The lengthening of the midlatitude and boreal fire seasons by up to 3 months presented in this study and the increased spread of fires to northern latitudes confirm results from the previous studies by *Spracklen et al.* [2009], *Moritz et al.* [2012], *de Groot et al.* [2013], and *Flannigan et al.* [2013], which were based on more simplified fire modeling approaches.

To our knowledge no references of future FRP estimates have been provided by other studies and the use of FRP as a diagnostic parameter in JSBACH-SPITFIRE is a novel approach. However, *de Groot et al.* [2013] applied three global climate models (GCMs) (CGCM3.1, HadCM3, and IPSL-CM4) to simulate fire activity and fire line intensity in Canada and Siberia between 2091 and 2100. Overall, the fire line intensity of individual fires was expected to increase substantially in the future. An increase in FRP in these regions is similarly projected in our simulations, but globally, only a weak shift toward more intense fires is found even for the RCP8.5 scenario.

The simulated future regional changes in boreal and midlatitude AOT due to changes in wildfire emissions show a magnitude which is similar to results presented by *Ward et al.* [2012]. But due to the differences in fire model representations, population density projections, and atmospheric conditions, the results of this study are only in line with the extratropical increase in AOT, not with the strong tropical increase in AOT shown by *Ward et al.* [2012].

In the vicinity of the major wildfire activity regions, wildfire-induced positive and negative changes in AOT of up to 50–100% are shown. Previous studies have shown that regional changes in wildfire aerosol concentrations of this magnitude can lead to a local suppression or intensification of convective precipitation [e.g., *Andreae et al.*, 2004; *Grell et al.*, 2011] and can even impact atmospheric large-scale systems like the Hadley circulation [*Tosca et al.*, 2013] and atmospheric convection patterns in tropical Africa [*Tosca et al.*, 2015].

With the next generation of Earth system models, fully coupled high resolution simulations will potentially provide more appropriate settings to study local vegetation wildfire-aerosol cloud interactions and potential feedbacks. Special attention should be paid to the investigation of changes in aerosol-cloud interactions in a future warmer climate as our results indicate strong regional changes in mean vertical aerosol profiles. The methodological approaches applied in this study, which link vegetation modeling, emission heights, and aerosol-climate modeling, may help to step forward toward a more accurate assessment of the future interactions between wildfires and climate.

Appendix A: Description of the FRP Distribution Scheme

In the original version of the SPITFIRE model by *Thonicke et al.* [2010] neither information on FRP nor on the attribution of FRP and emissions to individual fires is included. As described in section 2.1, we introduced the diagnostic variable FRP of all fires within a grid cell in JSBACH-SPITFIRE. In addition, we developed an empirical-statistical scheme that aims to distribute the total FRP of a grid box to a given number of individual fires provided by JSBACH-SPITFIRE. Therefore, we first calculate a probability density function (PDF) of the FRP distribution to individual fires based on satellite-based GFASv1.2 data. We limit our analysis to FRP classes which bin FRP values in specific ranges, see section 2.3. The empirical-statistical FRP distribution scheme is

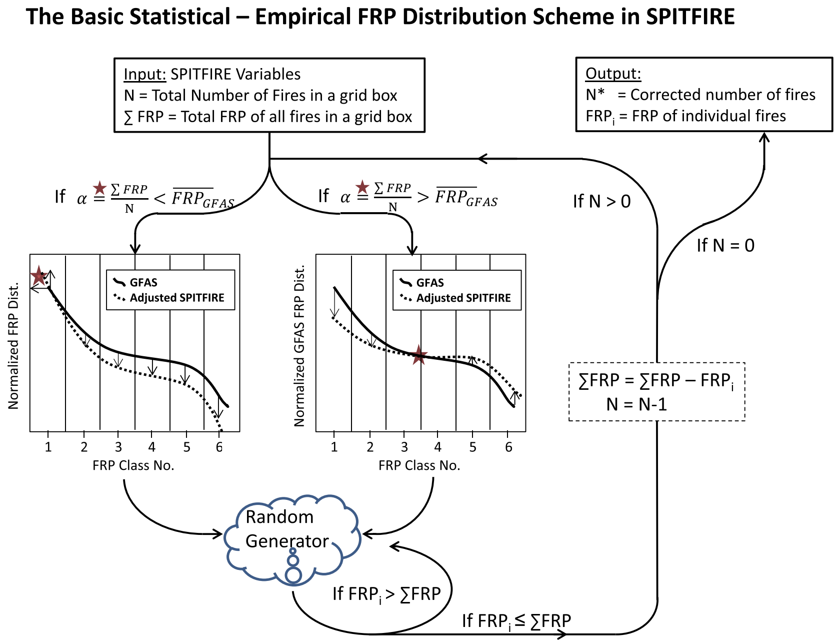

Figure A1. FRP distribution scheme applied in JSBACH-SPITFIRE. Note that the schematic drawing of the normalized FRP distribution includes only six FRP classes for reasons of clarity, but in reality 47 FRP classes are applied.

designed to achieve a JSBACH-SPITFIRE PDF which is similar to the PDF derived from GFAS data. To preserve the number of fires and the total FRP of a grid cell simulated by JSBACH-SPITFIRE, modifications have to be applied to the satellite-based GFAS PDF. This is done as follows.

We distribute the total FRP of all fires in a grid cell ($\sum$FRP) to individual FRP classes as described in Figure A1. First, we divide $\sum$FRP by the simulated number of fires N to get an FRP value for the assumption that all fires would have the same FRP. This FRP value α (see red star in Figure A1) is compared to the mean FRP value of an individual fire in GFAS, $\overline{\text{FRP}}_{\text{GFAS}}$. If α is larger than $\overline{\text{FRP}}_{\text{GFAS}}$, α represents the turning point of the subsequent PDF tuning (see right diagram in Figure A1). The PDF of all FRP classes larger than α is increased by a factor $\alpha/\overline{\text{FRP}}_{\text{GFAS}}$. All FRP classes smaller than α are decreased by a factor which scales the remaining FRP classes linearly in a way that the integral over the PDF remains 1, see upward and downward arrows right and left to the red star in Figure A1. If α is smaller than $\overline{\text{FRP}}_{\text{GFAS}}$, the upscaling and downscaling of FRP classes are applied in different directions as described before.

The updated PDF is used together with a random number generator to calculate a potential FRP of one specific fire. We then test whether the FRP of this fire is smaller or equal the total FRP of all fires $\sum$FRP in order to decide if the individual FRP is still consistent with the total FRP of a grid cell simulated by JSBACH-SPITFIRE. If the remaining $\sum$FRP would become negative, the random generator is run once again. Otherwise, the specific FRP is subtracted from the remaining $\sum$FRP and the number of fires N is reduced by 1. Thereafter, another iteration of the algorithm is started in case the number of fires is greater than zero. For the last remaining fire within a grid box, the total remaining FRP is automatically adjusted to the nearest FRP class value.

In rare cases where α is smaller than the FRP of class 1, the standard FRP distribution scheme would a priori be incapable to realistically allocate the number of fires simulated by JSBACH-SPITFIRE to individual FRP classes. Therefore, the FRP value of FRP class number 1 has to be adjusted. Here we apply an adjustment of FRP class 1 to a value of $0.25 \times \alpha$. The value of 0.25 is to some extend arbitrarily chosen, but our empirical test cases indicated a reasonable FRP distribution for this factor.

In order to save computational time in ECHAM6-HAM2, we apply a slightly modified FRP binning scheme as presented in *Veira et al.* [2015b]. This FRP class scheme summarizes individual fires of similar FRP in specific bins and runs the plume height parametrization only once for each bin. In contrast to the individual observational

Table A1. Description of the Applied FRP Binning Scheme Which Groups Fires of a Certain FRP Range[a]

FRP Bin Number	1–10	11–15	16-21	22–31	32–38	39–43	44–46	47
FRP range (MW)	0–100	100–200	200–500	500–1500	1500–5000	5000–10,000	10,000–25,000	25,000–50,000
Bin width (MW)	10	20	50	100	500	1000	5000	25,000

[a] Mean FRP bin values serve as input for the plume height parametrization applied in ECHAM6-HAM2.

FRP values of FRP bins 27–47 applied in *Veira et al.* [2015b], here the JSBACH-SPITFIRE FRP distribution scheme (see section 2.1) requires fixed FRP values for the FRP bins 27–47. Table A1 provides a summary of the FRP bin ranges and bin widths applied in the present study.

Appendix B: Analysis of Changes in Wildfire Activity

In the following, we make an attempt to analyze the main drivers for changes in wildfire emission fluxes in our JSBACH-SPITFIRE simulations. All changes refer to relative differences in total carbon emission fluxes between the JSBACH-SPITFIRE RCP scenarios 2.6, 4.5, and 8.5 for 2090–2099 compared to JSBACH-SPITFIRE PD emissions for 1996–2005. Region-specific analyses are carried out for six major biomass burning regions: Boreal North America, Temperate North America, the Amazon, Africa, Siberia, and Australia (see Figure 5). For these regions, we calculate Pearson correlation coefficients between changes in emission fluxes and changes in parameters which are assumed to be the driving forces of wildfires according to the fire process representations in JSBACH-SPITFIRE. The parameters chosen for the analysis are the number of human ignitions, the available fuel of fuel classes 1–100 h, the Fire Danger Index (FDI), and precipitation. The results of all parameter analyses are summarized in Table B1. As precipitation, fuel load and FDI are nonlinearly interdependent, the linear correlation analysis shown in this study represents only a rough first estimate of potential drivers for future fire activity. Furthermore, the analysis is limited to 10 year periods in which vegetation dynamics and internal climate variability are not accounted for.

Generally, the most significant and largest correlations can be detected for several regions and parameters for simulation RCP8.5 compared to the other two simulations. For RCP8.5, fuel availability is identified to be the major driver of extratropical changes in wildfire emissions. The large decrease in African emissions observed in RCP8.5 can primarily be attributed to a strong decrease in human ignition rates caused by land use change and

Table B1. Correlations Between Changes in Fire-Driving Parameters and Changes in Carbon Emission Fluxes 2090–2099 Versus 1996–2005[a]

Parameter	Temperate NA	Boreal NA	Siberia	Amazon	Australia	Africa
RCP2.6 Ignitions	(0.09)	(0.10)	(0.04)	(0.06)	(−0.10)	**0.45**
RCP2.6 Fuel 1–100 h	**0.19**	**0.46**	(0.02)	(0.06)	(−0.04)	**0.36**
RCP2.6 FDI	(−0.06)	**0.32**	(0.01)	(0.03)	(−0.03)	(−0.09)
RCP2.6 Precipitation	**0.17**	**−0.15**	(0.02)	(−0.06)	(0.11)	**0.32**
RCP4.5 Ignitions	(0.09)	(0.03)	(0.02)	(0.06)	(0.08)	(0.09)
RCP4.5 Fuel 1–100 h	(0.07)	(0.09)	(0.00)	(0.12)	(−0.11)	**0.30**
RCP4.5 FDI	(−0.01)	(0.06)	(−0.03)	(0.01)	(0.10)	**−0.34**
RCP4.5 Precipitation	(−0.07)	**−0.11**	(0.02)	**0.16**	(0.01)	**0.33**
RCP8.5 Ignitions	(−0.10)	(0.03)	(0.01)	(0.14)	**0.43**	**0.59**
RCP8.5 Fuel 1–100 h	**0.68**	**0.71**	**0.35**	(0.02)	**0.24**	(0.05)
RCP8.5 FDI	(0.01)	**0.39**	(−0.02)	**0.30**	**0.47**	(−0.06)
RCP8.5 Precipitation	**0.14**	(0.03)	(0.00)	(0.05)	**0.22**	**0.19**

[a] Numbers represent Pearson correlation coefficients. Bold numbers indicate that the given correlations are statistically significant at a 95% confidence interval. Numbers in brackets indicate that these correlations are statistically not significant at a 95% confidence interval.

increasing population density. A more sophisticated analysis would require an ensemble of separate model simulations with individually fixed parameters. But due to the high computational expenses of the long-term model experiments, these extensions go beyond the scope of the present study.

Appendix C: Future Changes in Dust, Sea Salt, and DMS Burdens

In section 3.7 the simulated future changes in AOT are discussed and compared to changes in atmospheric burdens of different aerosol species. In addition to the BC burden analysis provided in section 3.7, Figure C1 shows relative changes in dust, sea salt, and DMS burdens for the CLIMATE-ONLY simulation compared to PD-SPITFIRE.

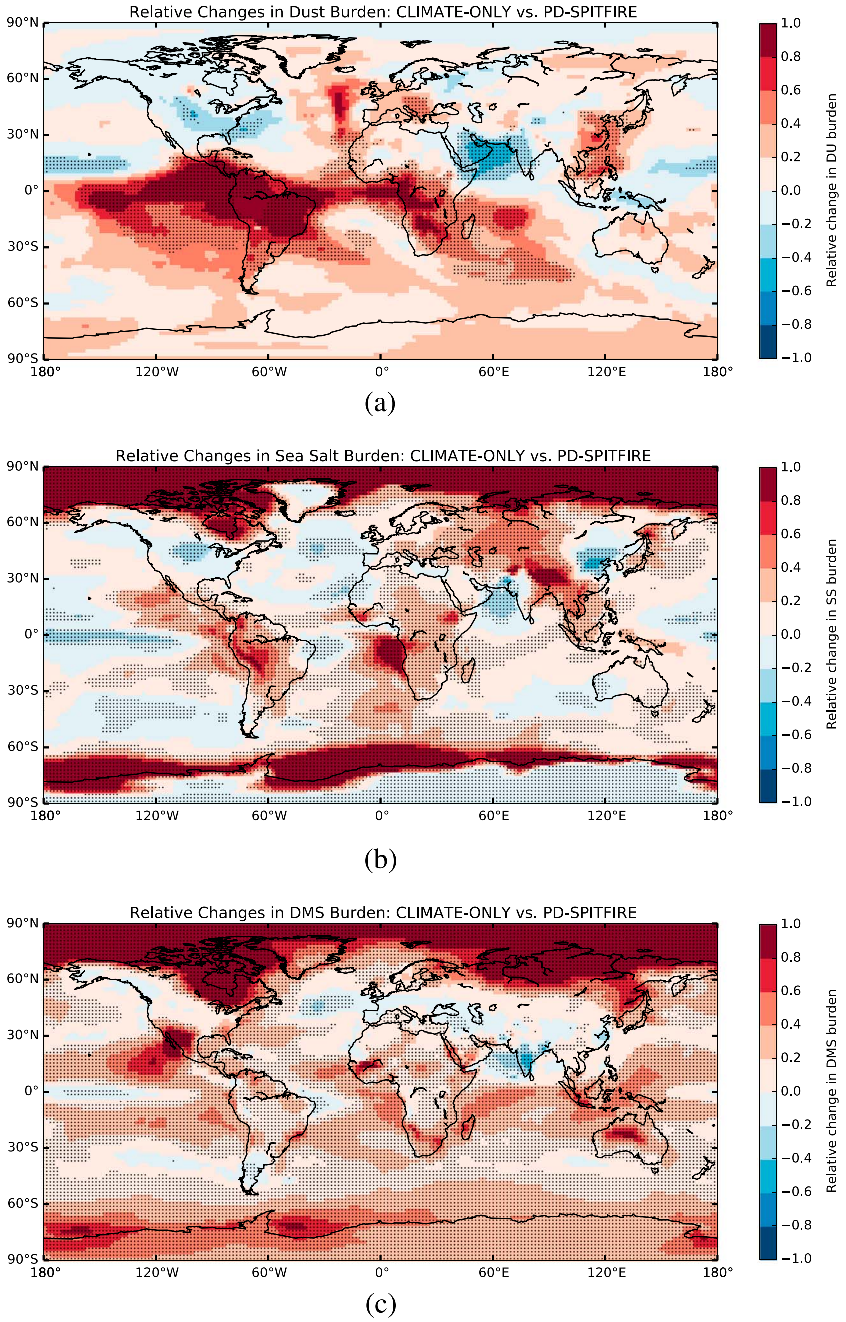

Figure C1. Relative changes in (a) dust, (b) sea salt, and (c) DMS burdens for simulation CLIMATE-ONLY (period 2090–2099) compared to the reference simulation PD-SPITFIRE based on the period 1996–2005. Black dots indicate significance of yearly means based on a student's *t* test at a 95% confidence interval.

Acknowledgments
The authors would like to thank the DFG for funding the Emmy-Noether junior research group "Fire in the Earth System." Furthermore, we acknowledge the critical and inspiring internal review by Stephan Bakan (Max Planck Institute for Meteorology, Hamburg). The satellite-based data set GFASv1.2 was provided by Samuel Remy (LMD, Paris) and Johannes Kaiser (Max Planck Institute for Chemistry, Mainz). The ECHAM-HAMMOZ model is developed by a consortium composed of ETH Zurich, Max Planck Institute for Meteorology, Forschungszentrum Juelich, University of Oxford, the Finnish Meteorological Institute and the Leibniz Institute for Tropospheric Research, and managed by the Center for Climate Systems Modeling (C2SM) at ETH Zurich. Primary data and scripts used in the analysis and other supplementary information that may be useful in reproducing the authors' work are archived by the Max Planck Institute for Meteorology and can be obtained by contacting publications@mpimet.mpg.de.

References

Akagi, S. K., R. J. Yokelson, C. Wiedinmyer, M. J. Alvarado, J. S. Reid, T. Karl, J. D. Crounse, and P. O. Wennberg (2011), Emission factors for open and domestic biomass burning for use in atmospheric models, *Atmos. Chem. Phys.*, *11*(9), 4039–4072, doi:10.5194/acp-11-4039-2011.

Andreae, M., and P. Merlet (2001), Emission of trace gases and aerosols from biomass burning, *Global Biogeochem. Cycles*, *15*(4), 955–966.

Andreae, M. O., D. Rosenfeld, P. Artaxo, A. A. Costa, G. P. Frank, K. M. Longo, and M. A. F. Silva-Dias (2004), Smoking rain clouds over the Amazon, *Science*, *303*(5662), 1337–1342, doi:10.1126/science.1092779.

Andrews, P. (2009), *BehavePlus Fire Modeling System, Version 5.0: Variables*, Rocky Mountain Research Station Publishing Services, 111 pp., Fort Collins, Colo.

Bond, T. C., C. Zarzycki, M. G. Flanner, and D. M. Koch (2011), Quantifying immediate radiative forcing by black carbon and organic matter with the Specific Forcing Pulse, *Atmos. Chem. Phys.*, *11*(4), 1505–1525, doi:10.5194/acp-11-1505-2011.

Bond, T. C., et al. (2013), Bounding the role of black carbon in the climate system: A scientific assessment, *J. Geophys. Res. Atmos.*, *118*, 5380–5552, doi:10.1002/jgrd.50171.

Boucher, O., et al. (2013), *Clouds and Aerosols*, Book Section 7, pp. 571–657, Cambridge Univ. Press, Cambridge, U. K., and New York, doi:10.1017/CBO9781107415324.015.

Bowman, D. M. J. S., et al. (2009), Fire in the Earth system, *Science*, *324*(5926), 481–484, doi:10.1126/science.1163886.

Brovkin, V., L. Boysen, T. Raddatz, V. Gayler, A. Loew, and M. Claussen (2013), Evaluation of vegetation cover and land-surface albedo in MPI-ESM CMIP5 simulations, *J. Adv. Model. Earth Syst.*, *5*(1), 48–57, doi:10.1029/2012MS000169.

Carslaw, K. S., O. Boucher, D. V. Spracklen, G. W. Mann, J. G. L. Rae, S. Woodward, and M. Kulmala (2010), A review of natural aerosol interactions and feedbacks within the Earth system, *Atmos. Chem. Phys.*, *10*(4), 1701–1737, doi:10.5194/acp-10-1701-2010.

Chin, M., T. Diehl, O. Dubovik, T. F. Eck, B. N. Holben, A. Sinyuk, and D. G. Streets (2009), Light absorption by pollution, dust, and biomass burning aerosols: A global model study and evaluation with AERONET measurements, *Ann. Geophys.*, *27*(9), 3439–3464, doi:10.5194/angeo-27-3439-2009.

Chung, C. E., V. Ramanathan, and D. Decremer (2012), Observationally constrained estimates of carbonaceous aerosol radiative forcing, *Proc. Natl. Acad. Sci. U.S.A.*, *109*, 11,624–11,629, doi:10.1073/pnas.1203707109.

Ciais, P., et al. (2013), Carbon and Other Biogeochemical Cycles, book section 6, pp. 465–570, doi:10.1017/CBO9781107415324.015.

de Groot, W. J., M. D. Flannigan, and A. S. Cantin (2013), Climate change impacts on future boreal fire regimes, *Forest Ecol. Manage.*, *294*, 35–44, doi:10.1016/j.foreco.2012.09.027.

Dentener, F., et al. (2006), Nitrogen and sulfur deposition on regional and global scales: A multimodel evaluation, *Global Biogeochem. Cycles*, *20*, GB4003, doi:10.1029/2005GB002672.

Dickinson, K., and J. Kirkpatrick (1985), The flammability and energy content of some important plant species and fuel components in the forests of southeastern Tasmania, *J. Biogeogr.*, *12*(2), 121–134, doi:10.2307/2844836.

Flannigan, M., A. S. Cantin, W. J. de Groot, M. Wotton, A. Newbery, and L. M. Gowman (2013), Global wildland fire season severity in the 21st century, *Forest Ecol. Manage.*, *294*, 54–61, doi:10.1016/j.foreco.2012.10.022.

Flannigan, M. D., M. A. Krawchuk, W. J. de Groot, B. M. Wotton, and L. M. Gowman (2009), Implications of changing climate for global wildland fire, *Int. J. Wildland Fire*, *18*(5), 483–507, doi:10.1071/WF08187.

Freeborn, P. H., M. J. Wooster, W. M. Hao, C. a. Ryan, B. L. Nordgren, S. P. Baker, and C. Ichoku (2008), Relationships between energy release, fuel mass loss, and trace gas and aerosol emissions during laboratory biomass fires, *J. Geophys. Res.*, *113*, D01301, doi:10.1029/2007JD008679.

Giorgetta, M. A., et al. (2013), Climate and carbon cycle changes from 1850 to 2100 in MPI-ESM simulations for the Coupled Model Intercomparison Project phase 5, *J. Adv. Model. Earth Syst.*, *5*(3), 572–597, doi:10.1002/jame.20038.

Goldewijk, K. (2001), Estimating global land use change over the past 300 years: The HYDE database, *Global Biogeochem. Cycles*, *15*(2), 417–433, doi:10.1029/1999GB001232.

Grell, G., S. R. Freitas, M. Stuefer, and J. Fast (2011), Inclusion of biomass burning in WRF-Chem: Impact of wildfires on weather forecasts, *Atmos. Chem. Phys.*, *11*(11), 5289–5303, doi:10.5194/acp-11-5289-2011.

Hantson, S., G. Lasslop, S. Kloster, and E. Chuvieco (2015), Anthropogenic effects on global mean fire size, *Int. J. Wildland Fire*, *24*, 589–596, doi:10.1071/WF14208.

Huijnen, V., et al. (2012), Hindcast experiments of tropospheric composition during the summer 2010 fires over western Russia, *Atmos. Chem. Phys.*, *12*(9), 4341–4364, doi:10.5194/acp-12-4341-2012.

Hurrell, J. W., J. J. Hack, D. Shea, J. M. Caron, and J. Rosinski (2008), A new sea surface temperature and sea ice boundary dataset for the Community Atmosphere Model, *J. Clim.*, *21*(19), 5145–5153, doi:10.1175/2008JCLI2292.1.

Hurtt, G. C., et al. (2011), Harmonization of land-use scenarios for the period 1500-2100: 600 years of global gridded annual land-use transitions, wood harvest, and resulting secondary lands, *Clim. Change*, *109*(1–2), 117–161, doi:10.1007/s10584-011-0153-2.

Jones, A., J. M. Haywood, and O. Boucher (2007), Aerosol forcing, climate response and climate sensitivity in the Hadley Centre climate model, *J. Geophys. Res. Atmos.*, *112*, D20211, doi:10.1029/2007JD008688.

Joshi, M. M., J. M. Gregory, M. J. Webb, D. M. H. Sexton, and T. C. Johns (2007), Mechanisms for the land/sea warming contrast exhibited by simulations of climate change, *Clim. Dyn.*, *30*(5), 455–465, doi:10.1007/s00382-007-0306-1.

Kaiser, J. W., et al. (2012), Biomass burning emissions estimated with a global fire assimilation system based on observed fire radiative power, *Biogeosciences*, *9*(1), 527–554, doi:10.5194/bg-9-527-2012.

Keane, R. E. (2015), *Wildland Fuel Fundamentals and Applications*, Springer Int. Publ., Switzerland, doi:10.1007/978-3-319-09015-3.

Keywood, M., M. Kanakidou, A. Stohl, F. Dentener, G. Grassi, C. P. Meyer, K. Torseth, D. Edwards, A. M. Thompson, U. Lohmann, and J. Burrows (2013), Fire in the Air: Biomass burning impacts in a changing climate, *Crit. Rev. Environ. Sci. Technol.*, *43*, 40–83.

Klein Goldewijk, K., and P. H. Verburg (2013), Uncertainties in global-scale reconstructions of historical land use: An illustration using the HYDE data set, *Landscape Ecol.*, *28*(5), 861–877, doi:10.1007/s10980-013-9877-x.

Kloster, S., N. M. Mahowald, J. T. Randerson, and P. J. Lawrence (2012), The impacts of climate, land use, and demography on fires during the 21st century simulated by CLM-CN, *Biogeosciences*, *9*, 509–525, doi:10.5194/bg-9-509-2012.

Knorr, W., L. Jiang, and A. Arneth (2015), Climate, CO2, and demographic impacts on global wildfire emissions, *Biogeosci. Discuss.*, *12*, 15,011–15,050, doi:10.5194/bgd-12-15011-2015.

Kremens, R., M. Dickinson, and A. Bova (2012), Radiant flux density, energy density and fuel consumption in mixed-oak forest surface fires, *Int. J. Wildland Fire*, *21*, 722–730, doi:10.1071/WF10143.

Lamarque, J.-F., G. P. Kyle, M. Meinshausen, K. Riahi, S. J. Smith, D. P. van Vuuren, A. J. Conley, and F. Vitt (2011), Global and regional evolution of short-lived radiatively-active gases and aerosols in the Representative Concentration Pathways, *Clim. Change*, *109*(1–2), 191–212, doi:10.1007/s10584-011-0155-0.

Langmann, B., B. Duncan, C. Textor, J. Trentmann, and G. R. van der Werf (2009), Vegetation fire emissions and their impact on air pollution and climate, *Atmos. Environ.*, *43*(1), 107 – 116, doi:10.1016/j.atmosenv.2008.09.047.

Lasslop, G., K. Thonicke, and S. Kloster (2014), SPITFIRE within the MPI Earth system model: Model development and evaluation, *J. Adv. Model. Earth Syst.*, *6*, 740 – 755, doi:10.1002/2013MS000284.

Liu, Y., J. Stanturf, and S. Goodrick (2010), Trends in global wildfire potential in a changing climate, *Forest Ecol. Manage.*, *259*(4), 685 – 697, doi:10.1016/j.foreco.2009.09.002.

Lohmann, U., P. Stier, C. Hoose, S. Ferrachat, S. Kloster, E. Roeckner, and J. Zhang (2007), Cloud microphysics and aerosol indirect effects in the global climate model ECHAM5-HAM, *Atmos. Chem. Phys.*, *7*(13), 3425 – 3446, doi:10.5194/acp-7-3425-2007.

Luderer, G., J. Trentmann, T. Winterrath, C. Textor, M. Herzog, H. F. Graf, and M. O. Andreae (2006), Modeling of biomass smoke injection into the lower stratosphere by a large forest fire (Part II): Sensitivity studies, *Atmos. Chem. Phys.*, *6*(4), 5261 – 5277, doi:10.5194/acpd-6-6081-2006.

Luo, L., Y. Tang, S. Zhong, X. Bian, and W. E. Heilman (2013), Will future climate favor more erratic wildfires in the western United States?, *J. Appl. Meteorol. Climatol.*, *52*(11), 2410 – 2417, doi:10.1175/JAMC-D-12-0317.1.

Matichuk, R. I., P. R. Colarco, J. a. Smith, and O. B. Toon (2008), Modeling the transport and optical properties of smoke plumes from South American biomass burning, *J. Geophys. Res.*, *113*, D07208, doi:10.1029/2007JD009005.

Morandini, F., Y. Perez-Ramirez, V. Tihay, P.-A. Santoni, and T. Barboni (2013), Radiant, convective and heat release characterization of vegetation fire, *Int. J. Thermal Sci.*, *70*, 83 – 91, doi:10.1016/j.ijthermalsci.2013.03.011.

Moritz, M., M. Parisien, and E. Batllori (2012), Climate change and disruptions to global fire activity, *Ecosphere*, *3*, 1 – 22.

Myhre, G., T. F. Berglen, M. Johnsrud, C. R. Hoyle, T. K. Berntsen, S. A. Christopher, and D. W. Fahey (2009), Modelled radiative forcing of the direct aerosol effect with multi-observation evaluation, *Atmos. Chem. Phys.*, *9*(4), 1365 – 1392.

Pechony, O., and D. T. Shindell (2010), *Proc. Natl. Acad. Sci. U.S.A.*, *107*(45), 19,167 – 70, doi:10.1073/pnas.1003669107.

Penrod, A., Y. Zhang, K. Wang, S.-Y. Wu, and L. R. Leung (2014), Impacts of future climate and emission changes on U.S. air quality, *Atmos. Environ.*, *89*, 533 – 547, doi:10.1016/j.atmosenv.2014.01.001.

Petrenko, M., R. Kahn, M. Chin, A. Soja, and T. Kucsera (2012), The use of satellite-measured aerosol optical depth to constrain biomass burning emissions source strength in the global model GOCART, *J. Geophys. Res.*, *117*, D18212, doi:10.1029/2012JD017870.

Pfeiffer, M., a. Spessa, and J. O. Kaplan (2013), A model for global biomass burning in preindustrial time: LPJ-LMfire (v1.0), *Geosci. Model Dev.*, *6*(3), 643 – 685, doi:10.5194/gmd-6-643-2013.

Reichstein, M., et al. (2013), Climate extremes and the carbon cycle, *Nature*, *500*(7462), 287 – 895, doi:10.1038/nature12350.

Reick, C. H., T. Raddatz, V. Brovkin, and V. Gayler (2013), Representation of natural and anthropogenic land cover change in MPI-ESM, *J. Adv. Model. Earth Syst.*, *5*(3), 459 – 482, doi:10.1002/jame.20022.

Reid, A. M., and K. M. Robertson (2012), Energy content of common fuels in upland pine savannas of the south-eastern US and their application to fire behaviour modelling, *Int. J. Wildland Fire*, *21*, 591 – 595, doi:10.1071/WF10139.

Roberts, G., M. J. Wooster, G. L. W. Perry, N. Drake, L.-M. Rebelo, and F. Dipotso (2005), Retrieval of biomass combustion rates and totals from fire radiative power observations: Application to southern Africa using geostationary SEVIRI imagery, *J. Geophys. Res.*, *110*, D21111, doi:10.1029/2005JD006018.

Samset, B. H., et al. (2013), Black carbon vertical profiles strongly affect its radiative forcing uncertainty, *Atmos. Chem. Phys.*, *13*(5), 2423 – 2434, doi:10.5194/acp-13-2423-2013.

Schneck, R., C. H. Reick, and T. Raddatz (2013), Land contribution to natural CO2 variability on time scales of centuries, *J. Adv. Model. Earth Syst.*, *5*(2), 354 – 365, doi:10.1002/jame.20029.

Schwarz, J. P., B. H. Samset, A. E. Perring, J. R. Spackman, R. S. Gao, P. Stier, M. Schulz, F. L. Moore, E. A. Ray, and D. W. Fahey (2013), Global-scale seasonally resolved black carbon vertical profiles over the Pacific, *Geophys. Res. Lett.*, *40*, 5542 – 5547, doi:10.1002/2013GL057775.

Shindell, D. T., et al. (2013), Radiative forcing in the ACCMIP historical and future climate simulations, *Atmos. Chem. Phys.*, *13*(6), 2939 – 2974, doi:10.5194/acp-13-2939-2013.

Smith, A. M. S., W. T. Tinkham, D. P. Roy, L. Boschetti, R. L. Kremens, S. S. Kumar, A. M. Sparks, and M. J. Falkowski (2013), Quantification of fuel moisture effects on biomass consumed derived from fire radiative energy retrievals, *Geophys. Res. Lett.*, *40*(23), 6298 – 6302, doi:10.1002/2013GL058232.

Sofiev, M., T. Ermakova, and R. Vankevich (2012), Evaluation of the smoke-injection height from wild-land fires using remote-sensing data, *Atmos. Chem. Phys.*, *12*(4), 1995 – 2006, doi:10.5194/acp-12-1995-2012.

Spracklen, D. V., L. J. Mickley, J. a. Logan, R. C. Hudman, R. Yevich, M. D. Flannigan, and a. L. Westerling (2009), Impacts of climate change from 2000 to 2050 on wildfire activity and carbonaceous aerosol concentrations in the western United States, *J. Geophys. Res.*, *114*, D20301, doi:10.1029/2008JD010966.

Stavros, E. N., D. McKenzie, and N. Larkin (2014), The climate-wildfire-air quality system: Interactions and feedbacks across spatial and temporal scales, *WIREs Clim. Change*, *5*(6), 719 – 733, doi:10.1002/wcc.303.

Stevens, B., et al. (2013), Atmospheric component of the MPI-M Earth System Model: ECHAM6, *J. Adv. Model. Earth Syst.*, *5*(2), 146 – 172, doi:10.1002/jame.20015.

Stier, P., J. Feichter, S. Kinne, S. Kloster, E. Vignati, J. Wilson, L. Ganzeveld, I. Tegen, and M. Werner (2005), The aerosol-climate model ECHAM5-HAM, *Atmos. Chem. Phys.*, *5*(4), 1125 – 1156, doi:10.5194/acp-5-1125-2005.

Thonicke, K., A. Spessa, I. C. Prentice, S. P. Harrison, L. Dong, and C. Carmona-Moreno (2010), The influence of vegetation, fire spread and fire behaviour on biomass burning and trace gas emissions: Results from a process-based model, *Biogeosciences*, *7*(6), 1991 – 2011, doi:10.5194/bg-7-1991-2010.

Tosca, M., J. Randerson, C. S. Zender, M. G. Flanner, and P. J. Rasch (2010), Do biomass burning aerosols intensify drought in equatorial Asia during El Niño?, *Atmos. Chem. Phys.*, *10*, 3515 – 3528, doi:10.5194/acp-10-3515-2010.

Tosca, M. G., J. T. Randerson, and C. S. Zender (2013), Global impact of smoke aerosols from landscape fires on climate and the Hadley circulation, *Atmos. Chem. Phys.*, *13*(10), 5227 – 5241, doi:10.5194/acp-13-5227-2013.

Tosca, M. G., D. J. Diner, M. J. Garay, and O. V. Kalashnikova (2015), Human-caused fires limit convection in tropical Africa, *Geophys. Res. Lett.*, *42*, 6492 – 6501, doi:10.1002/2015GL065063.1.

Unger, N., T. C. Bond, J. S. Wang, D. M. Koch, S. Menon, D. T. Shindell, and S. Bauer (2010), Attribution of climate forcing to economic sectors, *Proc. Natl Acad. Sci. U.S.A.*, *107*(8), 3382 – 3387, doi:10.1073/pnas.0906548107.

van der Werf, G. R., J. T. Randerson, L. Giglio, G. J. Collatz, M. Mu, P. S. Kasibhatla, D. C. Morton, R. S. DeFries, Y. Jin, and T. T. van Leeuwen (2010), Global fire emissions and the contribution of deforestation, savanna, forest, agricultural, and peat fires (1997-2009), *Atmos. Chem. Phys.*, *10*(23), 11,707 – 11,735, doi:10.5194/acp-10-11707-2010.

van Vuuren, D. P., and T. R. Carter (2014), Climate and socio-economic scenarios for climate change research and assessment: Reconciling the new with the old, *Clim. Change*, *122*(3), 415–429, doi:10.1007/s10584-013-0974-2.

van Vuuren, D. P., et al. (2011), The representative concentration pathways: An overview, *Clim. Change*, *109*(1–2), 5–31, doi:10.1007/s10584-011-0148-z.

Veira, A., S. Kloster, N. A. J. Schutgens, and J. W. Kaiser (2015a), Fire emission heights in the climate system—Part 2: Impact on transport, black carbon concentrations and radiation, *Atmos. Chem. Phys.*, *15*(13), 7173–7193, doi:10.5194/acp-15-7173-2015.

Veira, A., S. Kloster, S. Wilkenskjeld, and S. Remy (2015b), Fire emission heights in the climate system—Part 1: Global plume height patterns simulated by ECHAM6-HAM2, *Atmos. Chem. Phys.*, *15*(13), 7155–7171, doi:10.5194/acp-15-7155-2015.

von Hardenberg, J., L. Vozella, C. Tomasi, V. Vitale, a. Lupi, M. Mazzola, T. P. C. van Noije, a. Strunk, and a. Provenzale (2012), Aerosol optical depth over the Arctic: A comparison of ECHAM-HAM and TM5 with ground-based, satellite and reanalysis data, *Atmos. Chem. Phys.*, *12*(15), 6953–6967, doi:10.5194/acp-12-6953-2012.

Ward, D. S., S. Kloster, N. M. Mahowald, B. M. Rogers, J. T. Randerson, and P. G. Hess (2012), The changing radiative forcing of fires: Global model estimates for past, present and future, *Atmos. Chem. Phys.*, *12*(22), 10,857–10,886, doi:10.5194/acp-12-10857-2012.

Wooster, M. J., G. Roberts, G. L. W. Perry, and Y. J. Kaufman (2005), Retrieval of biomass combustion rates and totals from fire radiative power observations: FRP derivation and calibration relationships between biomass consumption and fire radiative energy release, *J. Geophys. Res.*, *110*, D24311, doi:10.1029/2005JD006318.

Yue, C., et al. (2014), Modelling the role of fires in the terrestrial carbon balance by incorporating SPITFIRE into the global vegetation model ORCHIDEE—Part 1: Simulating historical global burned area and fire regimes, *Geosci. Model Dev.*, *7*(6), 2747–2767, doi:10.5194/gmd-7-2747-2014.

Yue, C., P. Ciais, P. Cadule, K. Thonicke, and T. T. van Leeuwen (2015), Modelling the role of fires in the terrestrial carbon balance by incorporating SPITFIRE into the global vegetation model ORCHIDEE—Part 2: Carbon emissions and the role of fires in the global carbon balance, *Geosci. Model Dev.*, *8*(5), 1321–1338, doi:10.5194/gmd-8-1321-2015.

Zhang, F., J. Wang, C. Ichoku, E. J. Hyer, Z. Yang, C. Ge, S. Su, X. Zhang, S. Kondragunta, J. W. Kaiser, C. Wiedinmyer, and A. da Silva (2014), Sensitivity of mesoscale modeling of smoke direct radiative effect to the emission inventory: A case study in northern sub-Saharan African region, *Environ. Res. Lett.*, *9*(7), 75002, doi:10.1088/1748-9326/9/7/075002.

Zhang, K., et al. (2012), The global aerosol-climate model ECHAM-HAM, version 2: Sensitivity to improvements in process representations, *Atmos. Chem. Phys.*, *12*(19), 8911–8949, doi:10.5194/acp-12-8911-2012.